NAL TR-1357T

NAL Technical Report TR-1357T

ISSN 0389-4010
UDC 527.62
629.78
510.66

TECHNICAL REPORT OF NATIONAL AEROSPACE LABORATORY

TR-1357T

Development of Kinematic GPS Software, KINGS, and Flight Test Evaluation

Toshiaki Tsujii, Masaaki Murata, Masatoshi Harigae,
Takatsugu Ono and Toshiharu Inagaki

OCTOBER 1998

NATIONAL AEROSPACE LABORATORY

CHŌFU, TOKYO, JAPAN

Table of Contents

Development of Kinematic GPS Software, KINGS, and Flight Test Evaluation*

Toshiaki Tsujii*1 Masaaki Murata*2 Masatoshi Harigae*1
Takatsugu Ono*3 and Toshiharu Inagaki*3

ABSTRACT

Precise positioning using GPS carrier phase measurement has been widely used in static applications, i.e., geodetic surveying. However, it can also be applied to the precise positioning of a moving platform if an ambiguity contained in the GPS carrier phase measurement is resolved during the motion. The technique to resolve the ambiguity on the way/fly, which is called the OTF (On-the-Fly), has been investigated by many authors. In this paper, a new OTF algorithm is proposed and its feasibility for several kinds of applications is demonstrated.

The differential GPS positioning using carrier phase measurements is called Kinematic GPS (KGPS). We have developed our own Kinematic GPS Software, KINGS, in which the OTF is the most significant algorithm, and have evaluated its performance by conducting a lot of flight experiments using a research aircraft of the National Aerospace Laboratory (NAL). As a result, the correct ambiguity was resolved nearly instantaneously with more than 98% probability when the distance between the aircraft receiver and the ground reference receiver was less than 20km, and five or more satellites were observed. Once the ambiguity was resolved, the aircraft position was determined within 10cm (3σ).

Keywords: ambiguity resolution On-the-Fly, kinematic GPS, flight experiment, dual frequency

概　要

GPS搬送波位相干渉法による精密測位は、従来測地測量など静止基線解析の分野で幅広く応用されているが、時々刻々と変化する基線に対しては適用が難しいとされてきた。ところが、近年、搬送波に内在する未知数（アンビギティ）を実時間で解くアルゴリズム（On-the-Flyアルゴリズム）が多くの研究者によって開発され、移動体に対する精密測位も可能となってきた。本報告では、航技研で独自に開発した新しいOTFアルゴリズムを提案し、様々な実験による実証例を示す。

GPS搬送波を用いた移動体の精密測位は、キネマティックGPS(KGPS)とよばれるが、航技研では、独自のOTFアルゴリズムを核とするKGPSソフトウエア、KINGSを開発し、その性能評価を研究用航空機ドルニエ228を用いて行った。その結果、基線長20km以内、可視衛星５衛星以上の場合に、98%以上の確率でほぼ瞬時にアンビギティを解くことができた。アンビギティが正しく解けた場合の測位精度は約10cm (3σ)である。

＊　平成10年3月3日受付　(received 3 March 1998)
＊1　制御部 (Control Systems Division)
＊2　企画室 (Planning Office)
＊3　飛行実験部 (Flight Research Division)

Table of Symbols

PR	pseudorange
$\boldsymbol{\phi}$	carrier phase
c	light speed
t, t_{SV}	time of signal reception by the receiver, and the signal transmtting time from the satellite
T, T_{SV}	the reception and transmission time in GPS time
$\mathbf{R}$, $\mathbf{R}_{SV}$	position of receiver and satellite in the inertial space
$\mathbf{r}$, $\mathbf{r}_{SV}$	position of receiver and satellite in WGS 84
$\mathbf{r}^*_{SV}$	the satellite position calculated using the adopted ephemeris
$\boldsymbol{\rho}$	geometrical distance from the receiver to the satellite
$\boldsymbol{\rho}^*$	geometrical distance calculated using the adopted ephemeris
b, b_{SV}	clock bias of receiver and satellite
d_{ion}	ionospheric propagation delay (for L1 pseudorange)
d_{trop}	tropospheric propagation delay
d_{sag}	sagnac effect
d_{eph}	ephemeris error
I	parameter concerning the ionospheric delay
d_m	multipath error
$d_{m,\,phase}$	multipath error of carrier phase
N	integer ambiguity
$\boldsymbol{\varepsilon}$	measurement noise of carrier phase
$\boldsymbol{\varepsilon}_{PR}$	measurement noise of pseudorange
f	frequency of carrier phase
$\boldsymbol{\lambda}$	wavelength of carrier phase
$\boldsymbol{\Delta}$	operator to take single difference of observable
$\boldsymbol{\Delta\nabla}$	operator to take double difference of observable
H	measurement matrix
DD_i	double differenced observable between the first and (i+1)-th satellite
$\boldsymbol{\rho}^{*i}_u$	distance from user receiver to i-th satellite
$\boldsymbol{\sigma}_m$	standard deviation of double differenced measurement error
$\boldsymbol{\sigma}_p$	standard deviation of double differenced positioning error
C	measurement error covariance matrix (for double difference)
C_{PR}	measurement error covariance matrix of smoothed pseudorange
$C_{\mathbf{W}}$	measurement error covariance matrix of widelane
C^W_N	covariance matrix of initially estimated widelane ambiguity
C^{L1}_N	covariance matrix of initially estimated L1 ambiguity
$\boldsymbol{\sigma}^W_N$	standard deviation of the initial estimate of double differenced widelane ambiguity
$\boldsymbol{\sigma}^{L1}_N$	standard deviation of the initial estimate of double differenced L1 ambiguity
$\boldsymbol{\sigma}^{PR}_m$	standard deviation of double differenced smoothed pseudorange measurement error
$\boldsymbol{\sigma}^W_m$	standard deviation of double differenced widelane measurement error
$\boldsymbol{\sigma}^{L1}_m$	standard deviation of double differenced L1 carrier measurement error
$\boldsymbol{\sigma}^{PR}_p$, $\boldsymbol{\sigma}^{PR}_H$, $\boldsymbol{\sigma}^{PR}_V$	standard deviation of 3-dimensional, horizontal, and vertical positioning error when using the smoothed pseudorange
$\boldsymbol{\sigma}^W_p$, $\boldsymbol{\sigma}^W_H$, $\boldsymbol{\sigma}^W_V$	standard deviation of 3-dimensional, horizontal, and vertical positioning error when using the widelane
$\boldsymbol{\sigma}^{L1}_p$, $\boldsymbol{\sigma}^{L1}_H$, $\boldsymbol{\sigma}^{L1}_V$	

	standard deviation of 3-dimensional, horizontal, and vertical positioning error when using the L1 carrier
σ_H^{PR-W}	standard deviation of the difference between the pseudorange-position and widelane-position in horizontal direction
σ_H^{W-L1}	standard deviation of the difference between the widelane -position and L1-position in horizontal direction
σ_H^{PR-L1}	standard deviation of the difference between the pseudorange -position and L1-position in horizontal direction
$\mathbf{r}^{PR}, \mathbf{r}^{W}, \mathbf{r}^{L1}$	position calculated using smoothed pseudorange, widelane, and L1 carrier
$SLIP$	index for the detection of cycle slip
$\mathbf{y}$	measurement vector
$\bar{\mathbf{y}}$	computed measurement vector
$\bar{\mathbf{r}}$	a priori position of the receiver
$\delta\mathbf{y}$	measurement residual vector
$\mathbf{e}$	measurement error vector
J	cost function
$\delta\hat{\mathbf{r}}$	weighted least squares estimate of the receiver position correction
$\mathbf{x}$	state vector in the Kalman filter
$\mathbf{r}, \mathbf{v}, \mathbf{a}$	position, velocity and acceleration of the receiver in WGS84
$\boldsymbol{\tau}, \mathbf{u}$	time constant and white noise in a Gauss-Markov process
F, B, Q	system dynamics matrix, driving matrix, and process noise matrix in the continuous Kalman filter
$\boldsymbol{\Phi}, G, Q'$	system transition matrix, driving matrix, and process noise matrix in the discrete Kalman filter
$\Delta\nabla I$	estimate of the double differenced ionospheric parameter
$\delta h_{ion,wide}$	estimate of horizontal positioning error due to the ionospheric delay when the widelane is used
$\delta v_{ion,wide}$	estimate of vertical positioning error due to the ionospheric delay when the widelane is used
A_D, A_R	amplitude of direct and reflected signals
ψ_D	phase of direct signal
ψ	phase shift of reflected signal
Θ	multipath error
α	damping factor of the reflection
$\Delta\nabla\bar{d}_{eph}$	estimate of double differenced broadcast ephemeris error
δh_{eph}	estimate of horizontal positioning error due to the broadcast ephemeris error
δv_{eph}	estimate of vertical positioning error due to the broadcast ephemeris error
l	baseline length

Abbreviations

A/L	Approach and Landing
A-S	Anti-Spoofing
C/A-code	Coarse/Acquisition-code
CEP	Circular Error Probable
DGPS	Differential GPS
DME	Distance Measurement Equipment
DoD	Department of Defense
DRMS	Distance Root Mean Square
ECEF	Earth Centered Earth Fixed
ENRI	Electric Navigation Research Institute
FDAS	Flight Data Acquisition System
GPS	Global Positioning system
INS	Inertial Navigation System

KGPS	Kinematic GPS
MLS	Microwave Landing System
NAL	National Aerospace Laboratory
OTF	On the Fly
P-code	Precise-code
PPS	Precise Positioning Service
PRN	Pseudo Random Noise
RCS	Runway Coordinate System
RDOP	Relative Dilution of Precision
SA	Selective Availability
SPS	Standard Positioning Service
VLBI	Very Long Baseline Interferometry
WGS84	World Geodetic System 1984

1. Introduction

The NAVSTAR GPS (NAVigation System with Time and Ranging Global Positioning System) is a satellite-based radio navigation system providing precise position and time information. At present (Feb. 1998), 26 satellites are operating, and usually 4 to 9 satellites can be observed from any spot on earth at one time. Moreover, it has the advantage of independence from meteorological conditions. Thus, GPS civil users have been rapidly increasing with the spread of low cost GPS receivers. GPS is most commonly used for navigation of all kinds of vehicle such as cars, ships, and aircraft. The accuracy is approximately 100m horizontally, and 150m vertically (3σ) if the GPS receiver is used stand alone. However, if GPS measurements from one or more reference receivers are used, the accuracy will be 2-5 m horizontally and 4-10m vertically, although it depends on the hardware and other conditions (See Chapter 2.1.1). This technique is called differential GPS (DGPS). In the stand-alone GPS and DGPS navigation, the code phase measurement is used. Code phase, which is commonly called pseudorange, is an unambiguous range between satellite and receiver with precision of from some tens of centimeters to a few meters depending on the hardware. We evaluated the performance of DGPS for aircraft or spacecraft positioning using real flight data[1)-6)].

On the other hand, one can measure carrier phase in addition to the code phase by receiving the transmitted navigation satellite signal. Carrier phase is an ambiguous range with precision of several millimeters. Carrier phase after ambiguities are resolved is called carrier range. The use of carrier range enables us to conduct highly precise positioning. This ability has already been demonstrated in surveying, and today this technique is known as interferometric surveying after Very Long Baseline Interferometry (VLBI). In interferometric surveying, the ambiguity in carrier phase is resolved in batch process using the whole measurement data at once. Two major methods of ambiguity resolution have been investigated, i.e., the least squares searching method[7)], and the ambiguity function method[8)]. However, these methods were proved to be equivalent[9)]. In the search algorithm, the initial vector between the user and reference receiver is determined first, and then the carrier phase ambiguities are determined by choosing the best fit to the measurements from a number of candidates. Figure 1-1 shows the so-called search cube in the ambiguity space (see Chapter 2.2). In the static survey, the ambiguity is resolved by making use

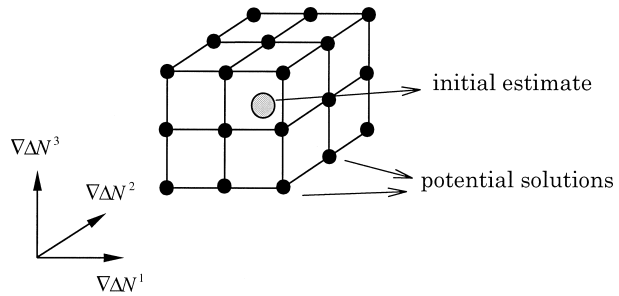

Figure 1-1 Search cube in ambiguity space

of the change of satellite constellation with time. Figure 1-2 shows the changes of positions corresponding to each ambiguity candidate according to the change of satellite constellation. Since the position solution corresponding to the correct ambiguity does not change with time, the ambiguity will be resolved after a considerable change of satellite constellation. Therefore, it is necessary to record the GPS measurement data until the constellation changes sufficiently. The time required for the resolution depends on the baseline length or other environmental conditions such as the ionospheric disturbance and multiple propagation effect. Typically, 15 to 30 minutes are necessary for 10km or shorter baselines while several hours are necessary for a few hundred baselines[10].

In addition to the geodetic survey, the precise (centimeter-level accuracy) carrier phase positioning has a wide area of application in aerospace technology such as precision approach, taxi guidance, and rendezvous docking. The carrier phase positioning of moving platforms with one or more reference GPS receivers is called Kinematic GPS (KGPS). Since the ambiguity is integer constant as long as the receiver maintains the lock of satellites, one can obtain the carrier range after the initial ambiguity resolution. Therefore, if the ambiguity is resolved by batch process in static mode before moving, which is called " static initialization ", the KGPS can be conducted until the receiver tracks four or more satellites continuously[11]. However, if some losses of locks (cycle slip) occur, or some satellites go out of sight, we cannot continue to perform the KGPS. So, in these applications the ambiguity resolution " on-the-fly " (OTF), i.e., without static initialization, is the key factor for precise positioning. A lot of authors have been investigating the OTF algorithm.

On the other hand, other kinds of positioning algorithms that make use of the carrier phase have been developed. For example, some authors treat the ambiguity as the real number and estimate the position by the Kalman filter, which is the so-called " Floating solution "[12], while the ambiguity is fixed as an integer in the OTF and the estimated solution is called " Fixed Solution ". However, its positioning accuracy (< 20cm) is inferior to the fixed solution by the OTF. Kleusberg developed a robust algorithm combining the pseudorange and the carrier doppler in which the integer ambiguity was not resolved[13]. The positioning accuracy was better than one meter, which was similar to the carrier smoothed solution. Nowadays, the fixed solution by the OTF is the most accurate kinematic solution.

When the P-code (Precision code, see Chapter 2.1.1) measurement was available and the baseline length was a few kilometers, the ambiguities in two frequencies were resolved by the so-called " extra-widelaning "[14]. However, once the A-S (Anti-Spoofing, see Chapter 2.1.1) was active, the searching method was applied more or less to the entire OTF algorithm. Most of the proposed OTF algorithms adopt the root sum squares as a statistical criterion in the search algorithm[9], [15]-[17]. This is called " test in the measurement domain ". On the other hand, another kind of criteria can be used, i.e., the position difference between the pseudorange-position (position solution estimated by using the pseudorange) and the position calculated by using each ambiguity candidate. This is called " test in the positioning domain ". Abidin et. al. proposed an OTF algorithm which adopted both criteria, and he considered the three dimensional position in the positioning domain test[18]. However, the vertical positioning accuracy is generally worse than the horizontal accuracy, and is affected by some error sources, especially ionospheric propagation delay. Therefore, we propose to use the horizontal position difference as a criterion in the positioning domain test. This method is very effective for dual frequency GPS receivers.

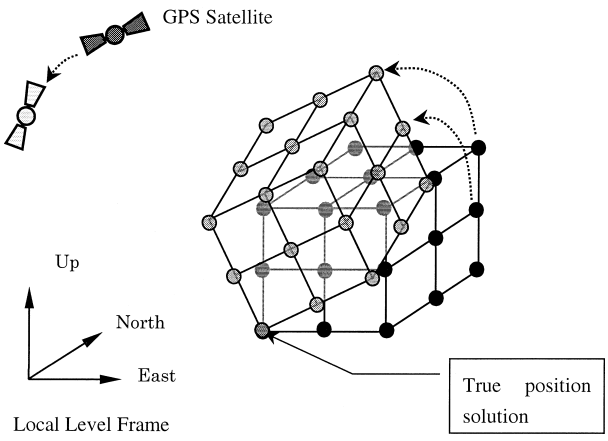

Figure 1-2 Changes of positions calculated using the ambiguity candidates in search cube

If the ambiguity can be resolved by the proposed OTF algorithm, several kinds of real time applications will be possible, such as precision navigation of vehicles and monitoring crustal movement during earthquakes. The attitude determination is also a probable application, in which more than one antenna are necessary onboard, but no ground reference receiver is required. Moreover, if we mounted some GPS antennas on a non-rigid platform, such as a space station, we could estimate not only its attitude but also the structural flexures. The objective of this paper is to evaluate the performance of the proposed OTF algorithm by flight experiments and to test the feasibility of its applications, i.e., aircraft precise positioning. In chapter 2, the OTF algorithm is described in detail. In chapter 3, the accuracy of carrier phase positioning is evaluated by analyzing static survey data in the Izu-Islands area. In order to estimate the dependence of accuracy on the distance between stations (baseline length), seven different baselines are used for analyses. Moreover, we estimate the limit baseline length at which the OTF performs successfully. Finally in that chapter, we demonstrate that crustal movement of a few centimeters during an earthquake can be detected by KGPS. In chapter 4, flight test configurations of KGPS is described and analytical results are reported. In these experiments, we used a research aircraft, Dornier 228-200 (Do-228), which belongs to the National Aerospace Laboratory (NAL) of Japan. Finally we conclude this study and describe some future works.

2. Algorithms of GPS Precise Positioning

In this chapter, the explicit forms of GPS observation equations are shown firstly, and the OTF algorithm is given next. Then the methods of cycle slip detection are described. And finally, the algorithms of KGPS positioning is shown, in which the OTF plays the most significant role. The analytical results using the real experimental data will be shown in Chapters 3 and 4.

2.1 Observation Equation

2.1.1 Pseudorange

The GPS satellite transmits microwave signals in two frequencies, i.e., L1 (1575.42MHz) and L2 (1227.60MHz). The L1 carrier phase is modulated by two kinds of Pseudo Random Noise (PRN), which are called Coarse/Acquisition (C/A) code and Precision (P) code, while the L2 carrier phase is modulated by P code. The L1 carrier phase is also modulated by the navigation message that contains the satellite orbit parameter (broadcast ephemeris). The main features of all three signals are given in Table 2-1, and Figure 2-1 shows how code and carrier are combined.

Since GPS is a military navigation system under primary responsibility of the U.S. Department of Defense (DoD), only limited access to the total system accuracy would be available to the civil user community. The service available to the civil

Table 2-1 GPS satellite signals

Atomic clock (Cs, Rb) fundamental frequency	10.23 MHz
L1 carrier signal	154 x 10.23 MHz
L1 frequency	1575.42 MHz
L1 wavelength	19.05 cm
L2 carrier signal	120 x 10.23 MHz
L2 frequency	1227.60 MHz
L2 wavelength	24.45 cm
P-code frequency (chipping rate)	10.23 MHz (Mbps)
P-code wavelength	29.31 m
P-code period	266 days; 7 days/satellite
C/A-code frequency (chipping rate)	1.023 MHz (Mbps)
C/A-code wavelength	293.1 m
C/A-code period	1 millisecond
data signal frequency	50 bps
data signal cycle length	30 seconds

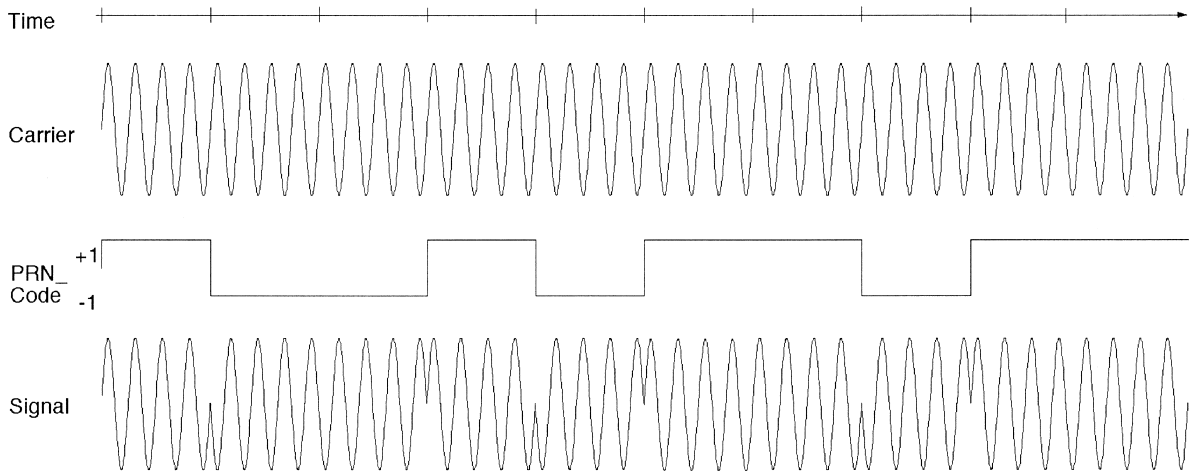

Figure 2-1 Structure of the GPS satellite signal

community is called Standard Positioning Service (SPS), while the service available to authorized (mainly military) users is called the Precise Positioning Service (PPS). Though C/A code is available for SPS users, the positioning accuracy will be degraded if the DoD operates the selective availability (SA). At present, SA is always active. In addition, when the Anti-Spoofing (A-S) is active, P code is changed to Y code that SPS users cannot access. The horizontal positioning accuracy for SPS and PPS users are given in Figure 2-2[10], in which the CEP (Circular Error Probable) for 50% probability and the 2DRMS (Distance Root Mean Square) for 95% probability are shown.

GPS receivers for navigation measure the propagation time from satellites to receivers using PRN codes and output the value of propagation time multiplied by the light speed ' c ' as a distance information between satellites and receivers. Since this value includes errors such as satellite and receiver clock, it is called " pseudorange ". The pseudorange (PR) is given as follows

$$PR = c(t - t_{SV}) + \varepsilon_{PR} \tag{2.1-1}$$

where t is the time of signal reception by the receiver, t_{SV} is the signal transmitting time from the satellite, and ε_{PR} is the measurement noise. Since t and t_{SV} are measured by the receiver clock and the satellite clock respectively, they have their own clock-derived error, called " clock bias ". Denoting the reception and transmission time in GPS time by T and T_{SV}, the clock biases of the receiver and satellite are

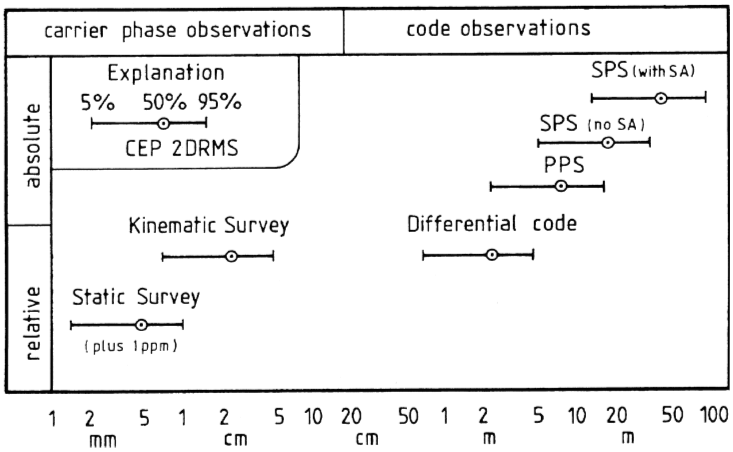

Figure 2-2 Horizontal positioning accuracy for SPS and PPS users

$$b=c(t-T)$$
$$b_{SV}=c(t_{SV}-T_{SV}) \tag{2.1-2}$$

Then Eq. (2.1-1) is rewritten as

$$\begin{aligned} PR&=c(t-T+T-T_{SV}+T_{SV}-t_{SV})+\boldsymbol{\varepsilon}_{PR}\\ &=c(t-T)+c(T-T_{SV})-c(t_{SV}-T_{SV})+\boldsymbol{\varepsilon}_{PR}\\ &=c(T-T_{SV})+b-b_{SV}+\boldsymbol{\varepsilon}_{PR} \end{aligned} \tag{2.1-3}$$

Denoting the position of receiver and satellite in the inertial space by $\mathbf{R}(T)$ and $\mathbf{R}_{SV}(T_{SV})$, the first term becomes

$$\begin{aligned} &c(T-T_{SV})=\boldsymbol{\rho}+d_{ion}+d_{trop}\\ &\boldsymbol{\rho}=|\mathbf{R}(T)-\mathbf{R}_{SV}(T_{SV})| \end{aligned} \tag{2.1-4}$$

where $\boldsymbol{\rho}$ is the geometrical distance from the receiver to the satellite, d_{ion} and d_{trop} are delays when the signal propagates through ionosphere and troposphere. Since the ionospheric delay depends on the total electron involved in the ionosphere, the delay for L1 pseudorange is written as

$$\begin{aligned} d_{ion}&=\frac{f_2}{f_1}I\\ I&=40.3\frac{\int N_e(s)ds}{f_1 f_2} \end{aligned} \tag{2.1-5}$$

where N_e is the density of electron, and f_1, f_2 are L1, L2 frequency. The electron density is integrated along the signal propagation path and higher orders are neglected. Though Eq. (2.1-4) is expressed in the inertial coordinates, the position and velocity of GPS receivers and satellites should be expressed in an ECEF (Earth Centered Earth Fixed) coordinate system, called "WGS84" (World Geodetic System 1984). Denoting the position of receiver and satellite in WGS 84 by $\mathbf{r}(T)$ and $\mathbf{r}_{SV}(T_{SV})$ respectively, the geometrical distance becomes

$$\boldsymbol{\rho}=|\mathbf{r}(T)-\mathbf{r}_{SV}(T_{SV})|+d_{sag} \tag{2.1-6}$$

d_{sag} shows a kind of special relativity effect, called "sagnac effect", where the propagation distance changes according to the earth rotation during the propagation. Sagnac effect is completely calculated using a mathematical equation[19]. Although $\mathbf{r}_{SV}(T_{SV})$ in Eq. (2.1-6) is the true position of a satellite, we can only estimate the position in WGS 84 using the broadcast ephemeris or precise ephemeris calculated by some organizations. Denoting the error of the ephemeris by d_{eph}, Eq. (2.1-4) is transformed to

$$\begin{aligned} \boldsymbol{\rho}&=|\mathbf{r}(T)-\mathbf{r}^*_{SV}(T_{SV})|+d_{sag}+d_{eph}\\ &=\boldsymbol{\rho}^*+d_{sag}+d_{eph} \end{aligned} \tag{2.1-7}$$

where $\mathbf{r}^*_{SV}$, $\boldsymbol{\rho}^*$ are the satellite position and geometrical distance calculated using the adopted ephemeris. From Eq. (2.1-3,4,7), the measurement equation of L1 pseudorange is written as follows

$$PR=\boldsymbol{\rho}^*+\frac{f_2}{f_1}I+d_{trop}+b-b_{SV}+d_{eph}+d_{sag}+\boldsymbol{\varepsilon}_{PR} \tag{2.1-8}$$

When SA is active, errors of satellite clock and broadcast ephemeris will be increased. Degrading the accuracy of broadcast ephemeris is called the $\boldsymbol{\varepsilon}$-process and dithering of the satellite clock is called the δ-process[19]. These errors will be included

in d_{eph} and b_{SV}. When there are some reflecting surfaces near the receiver such as streets, buildings, waterways, and vehicles, the measurement accuracy of pseudorange is affected by reflected signals. The effect caused by these indirect signals is called " multipath ". Multipath error, denoted by d_m, is very sensitive to the environment and sometimes reaches a few tens of meters for pseudorange. Adding the multipath error to Eq. (2.1-8) and removing the sagnac effect because it can be calculated exactly by a theoretical equation, the measurement equation of pseudorange is given as

$$PR=\rho^*+\frac{f_2}{f_1}I+d_{trop}+b-b_{SV}+d_{eph}+d_m+\varepsilon_{PR} \tag{2.1-9}$$

2. 1. 2 Carrier Phase

In the geodetic survey, carrier phase measurements are mainly used instead of the code phase measurements. This is because the measurement noise of the carrier phase is typically a few millimeters, while that of the code phase is a few meters generally. The carrier phase measured by the GPS receiver is the difference between the phase from the satellite at transmission time ($\theta_{SV}(t_{SV})$) and the phase generated by the receiver at reception time ($\theta(t)$). These phases are defined by the following equations[20), 21)]

$$\theta_{SV}(t_{SV})=ft_{SV} \tag{2.1-10}$$

$$\theta(t)=ft \tag{2.1-11}$$

where f is the frequency of the carrier and units are in cycles. In the above equations, the phases are defined to be zeros when the times are zeros in satellite and receiver clocks, respectively. Thus, the carrier phase ψ is described by

$$\psi(t)=f(t-t_{SV})+\varepsilon \tag{2.1-12}$$

where ε is the measurement noise. However, the observed carrier phase at the start time of measurement t_0 is only a fraction of the full wave. So, the observed carrier phase ψ_m is written as follows at the initial time:

$$\psi_m(t_0)=fr(\psi(t_0)) \tag{2.1-13}$$

$fr(\cdot)$ means that the fractional part of a wave is taken. Hence, the real carrier phase which contains unmeasured integer cycle, N, is written as follows

$$\psi(t_0)=\psi_m(t_0)-N \tag{2.1-14}$$

Since the carrier phase is integrated continuously unless a cycle slip occurs, the measured carrier phase at time t is given by

$$\psi_m(t)=\psi(t)-\psi(t_0)+\psi_m(t_0) \tag{2.1-15}$$

Substituting Eq. (2.1-14) for Eq. (2.1-15), the measured carrier phase is

$$\psi_m(t)=\psi(t)+N \tag{2.1-16}$$

Since $\psi(t)$ can be transformed like the pseudorange in Eq. (2.1-9), the measurement equation of the carrier phase is given by multiplying the wavelength λ by Eq. (2.1-16) and rewriting $\lambda\psi_m(t)$ tϕ as follows

$$\phi=\rho^*-\frac{f_2}{f_1}I+d_{trop}+b-b_{SV}+d_{eph}+d_{m,phase}+\lambda N+\varepsilon \tag{2.1-17}$$

In the above equations, the integer unknown N is called "ambiguity". $d_{m,\,phase}$ is the multipath error of the carrier phase, which is smaller than a few centimeters. Note that the sign of ionospheric delay is negative, while that for the pseudorange is positive.

In order to calculate the receiver position using these observables, it is important to reduce various kinds of errors in them. At first, the pseudorange should be smoothed using the carrier phase because the raw pseudorange is very noisy. In case of relative positioning with two or more receivers, a certain amount of these errors can be canceled by composing some kinds of linear combinations of the GPS data measured by the reference and user receivers.

2. 1. 3 Double Difference

At first, we compose the "single difference." When two receivers and one satellite are considered, the single difference of carrier phase for the satellite-i is defined as the difference between measurements by receiver-1 and receiver-2 (Figure 2-3):

$$\Delta\phi^i_{1,2}=\phi^i_1-\phi^i_2 \tag{2.1-18}$$

where subscripts denote the number of the receiver. Substituting Eq. (2.1-17) for Eq. (2.1-18), the result is

$$\Delta\phi=\Delta\rho^*-\frac{f_2}{f_1}\Delta I+\Delta d_{trop}+\Delta b+\Delta d_{eph}+\Delta d_{m,phase}+\lambda\Delta N+\Delta\varepsilon \tag{2.1-19}$$

The subscripts and superscript are omitted for simplicity.
The single difference of satellite clock bias is

$$b_{SV}(T_{SV1})-b_{SV}(T_{SV2})\cong \dot{b}_{SV}(T_{SV2})\cdot(T_{SV1}-T_{SV2}) \tag{2.1-20}$$

Since the satellite clock drift, $\dot{b}_{SV}$, is nominally smaller than 10^{-3} and the difference of transmitting time is negligibly small, the satellite clock biases cancel each other. If the baseline length between two receivers is small (up to some 20km), the signal propagation paths for both receivers are similar, then the ionospheric and tropspheric delays almost cancels and also the ephemeris error almost cancels. The effect of propagation delay depending on baseline length will be evaluated in Chapter 3.

Assuming two receivers 1,2, and two satellites, i, j, to be involved, two single differences for satellite-i and satellite-j are formed. The "double difference" is defined as the difference between these single differences (Figure 2-4). Denoting an operator to take the double difference by $\nabla\Delta$,

$$\nabla\Delta(\cdot)=(\cdot)^i_1-(\cdot)^j_1-(\cdot)^i_2+(\cdot)^j_2 \tag{2.1-21}$$

the double difference of the carrier phase is given as follows

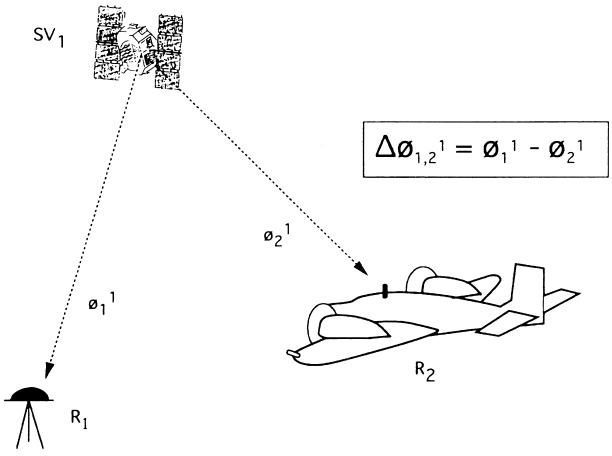

Figure 2-3 Single difference of GPS measurement

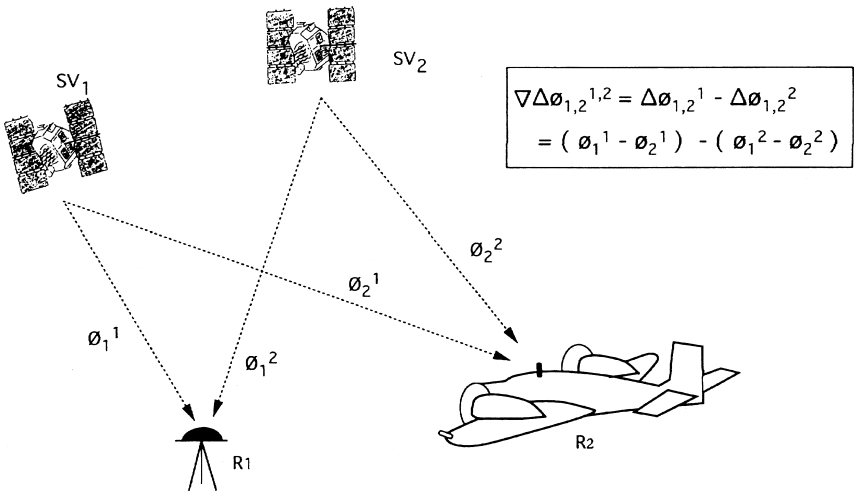

Figure 2-4 Double difference of GPS measurement

$$\nabla\Delta\phi = \nabla\Delta\rho^* - \frac{f_2}{f_1}\nabla\Delta I + \nabla\Delta d_{trop} + \nabla\Delta d_{eph} + \nabla\Delta d_{m,phase} + \lambda\nabla\Delta N + \nabla\Delta\varepsilon \tag{2.1-22}$$

The receiver clock biases cancel because the reception time of satellite-i and j signals are the same, so clock biases are also the same.

Moreover, taking the time difference between the double differences, the ambiguity is also canceled because it is a constant. This observable is called "triple difference":

$$\delta\nabla\Delta\phi = \delta\nabla\Delta\rho^* - \frac{f_2}{f_1}\delta\nabla\Delta I + \delta\nabla\Delta d_{trop} + \delta\nabla\Delta d_{eph} + \delta\nabla\Delta d_{m,phase} + \delta\nabla\Delta\varepsilon \tag{2.1-23}$$

When the observation rate is high and the ionosphere and troposphere are stable, the propagation delays may be negligible. If the initial position of a vehicle is known, positioning with triple difference is very easily carried out because it is not necessary to resolve ambiguities, i.e., the initialization can be omitted. However, the positioning accuracy will be degraded gradually because the estimated position at an epoch depends on the position at the previous epoch, so the positioning error will be accumulated. Furthermore, once a cycle slip occurs and the number of visible satellites becomes less than 4, the positioning cannot be performed anymore.

2. 1. 4 Linear Combinations of GPS Measurements

When a dual frequency GPS receiver is used, some kinds of linear combinations of GPS measurements can be formed which are useful for the OTF and cycle slip detection[22]. A linear combination of L1 and L2 carrier phases, which is called "widelane", is formed as follows

$$\Phi_W = \left(\frac{\Phi_1}{\lambda_1} - \frac{\Phi_2}{\lambda_2}\right)\frac{c}{f_1 - f_2}, \quad \begin{cases} \lambda_W = \dfrac{c}{f_1 - f_2} \cong 86.2cm \\ N_W = N_1 - N_2 \end{cases} \tag{2.1-24}$$

Subscript 1, 2, W denote L1, L2, and widelane observable. The double differenced widelane is

$$\nabla\Delta\phi_W = \nabla\Delta\rho + \nabla\Delta I + \nabla\Delta d_{trop} + \nabla\Delta d_{eph} + \nabla\Delta d_{m,W} + \lambda_W\nabla\Delta N_W + \nabla\Delta\varepsilon_W \tag{2.1-25}$$

Since the effective wavelength of widelane is about four times as large as L1 wavelength, to resolve widelane ambiguity is easier than for L1 ambiguity. However, the measurement noise becomes about three times as large as L1 noise and ionospheric delay error is enlarged by a factor of about 1.3 due to a coefficient $f_2/f_1 = 60/77 \cong 0.78$; therefore, the widelane is not

suited to the final positioning solution.

From the L1 and L2 carrier phases, a so-called " narrowlane " observable is also formed as

$$\Phi_N=\left(\frac{\Phi_1}{\lambda_1}+\frac{\Phi_2}{\lambda_2}\right)\frac{c}{f_1+f_2},\quad \begin{cases}\lambda_N=\dfrac{c}{f_1+f_2}\cong 10.7cm\\ N_N=N_1+N_2\end{cases} \tag{2.1-26}$$

The double differenced narrowlane is

$$\nabla\Delta\phi_N=\nabla\Delta\rho-\nabla\Delta I+\nabla\Delta d_{trop}+\nabla\Delta d_{eph}+\nabla\Delta d_{m,N}+\lambda_N\nabla\Delta N_N+\nabla\Delta\varepsilon_N \tag{2.1-27}$$

Since the effective wavelength is about half of the L1 wavelength, to resolve ambiguity is difficult. However, the measurement noise is about half of the L1 noise, so the narrowlane solution may be a final solution for short baseline applications when the enlarged ionospheric delay error is sufficiently small.

From the widelane and narrowlane observable, the ionospheric delay free (ion-free) observable is formed as follows

$$\Phi_{ion}=\frac{1}{2}(\Phi_W+\Phi_N) \tag{2.1-28}$$

The double differenced ion-free observable is

$$\nabla\Delta\phi_{ion}=\nabla\Delta\rho+\nabla\Delta d_{trop}+\nabla\Delta d_{eph}+\nabla\Delta d_{m,ion}+\frac{1}{2}(\lambda_W\nabla\Delta N_W+\lambda_N\nabla\Delta N_N)+\nabla\Delta\varepsilon_{ion} \tag{2.1-29}$$

Since the ionospheric delay cancels, this observable is suited to a long baseline application though the measurement noise is enlarged by a factor of about 3.

Finally, we introduce the so-called " ionospheric signal " as follows:

$$\begin{aligned}\Phi_I&=\Phi_N-\Phi_W\\&=-2I+\lambda_N N_N-\lambda_W N_W+(d_{m,N}-d_{m,W})+(\varepsilon_N-\varepsilon_W)\end{aligned} \tag{2.1-30}$$

When the ambiguities of widelane and narrowlane, i.e., L1 and L2 carrier phase, and multipath errors are sufficiently small, the amount of ionospheric delay can be evaluated using this ionospheric signal. Results of evaluation will be discussed in Chapter 3. Also, this is useful for the cycle slip detection (Chapter 2.3).

2. 2 Ambiguity Resolution On-the-Fly

The goal of ambiguity resolution is to determine the L1 ambiguity. However, the widelane ambiguity should be resolved beforehand because the position information calculated using widelane is used to determine the initial value of L1 ambiguity. Furthermore, the carrier-smoothed pseudorange is also used to determine the initial value of widelane ambiguity. Here, we give the observation equations of measurement data used in the OTF algorithm:

$$\nabla\Delta PR_1=\nabla\Delta\rho^*+\nabla\Delta\frac{f_2}{f_1}I+\nabla\Delta d_{trop}+\nabla\Delta d_{eph}+\nabla\Delta d_{m1}+\nabla\Delta\varepsilon_{PR1} \tag{2.2-1}$$

$$\nabla\Delta\phi_1=\nabla\Delta\rho^*-\nabla\Delta\frac{f_2}{f_1}I+\nabla\Delta d_{trop}+\nabla\Delta d_{eph}+\nabla\Delta d_{m1,phase}+\lambda_1\nabla\Delta N_1+\nabla\Delta\varepsilon_1 \tag{2.2-2}$$

$$\nabla\Delta\phi_W=\nabla\Delta\rho^*+\nabla\Delta I+\nabla\Delta d_{trop}+\nabla\Delta d_{eph}+\nabla\Delta d_{m,W}+\lambda_W\nabla\Delta N_W+\nabla\Delta\varepsilon_W \tag{2.2-3}$$

where subscripts in Eq. (2.2-1) and (2.2-2) denote that the terms are for L1 frequency. Using these data step by step, we finally resolve the L1 ambiguity, and obtain the positioning solution. Measurement errors of three observables are different, which are listed in Table 2-2. These values are calculated using the accumulated data in our flight test configuration where two

Table 2-2 Summary of measurement errors and corresponding position errors assuming RDOP = 3

Observable	Measurement error (cm)	position error (cm)
DD of carrier smoothed pseudorange	65	195
DD of widelane carrier phase	4	12
DD of L1 carrier phase	1	3

Trimble 4000SSE receivers were used. The reference receiver was connected to a Trimble Geodetic L1/L2 antenna with groundplane which mitigate the multipath error, while the onboard receiver was connected to a Tecom MIL-E-5400 antenna mounted on the roof of the Do-228 cockpit (see Chapter 4.1.1). Since the aircraft was on the ground about 200m away from the reference receiver, the propagation delays canceled and the ephemeris error was also negligible. However, the measurement error in Table 2-2 contains multipath error and measurement noise. We adopt these values as typical measurement errors in the OTF algorithm although they may slightly change with the circumstances; for example, when the aircraft banks deeply, their wings may become the reflecting surfaces and cause the multipath error. If we assumed the ideal condition such that there was no multipath effect, the measurement error would be the measurement noise. And if the measurement noise of the L1 carrier phase (～ 3mm for double differences) is almost the same as the L2 phase, the widelane measurement noise is about six times as large as the L1 measurement noise[23]. However, the widelane measurement noise is worse at the present because the L2 carrier phase measurement is noisier than the L1 carrier phase when the A-S is active.

The flowchart of OTF algorithm is shown in Figure 2-5. The details are described step by step as follows[24), 25)].

(1) The initial estimate of widelane ambiguities are determined by Eq. (2.2-4) using the position of the receiver which is calculated using the double differences of carrier smoothed L1 pseudoranges.

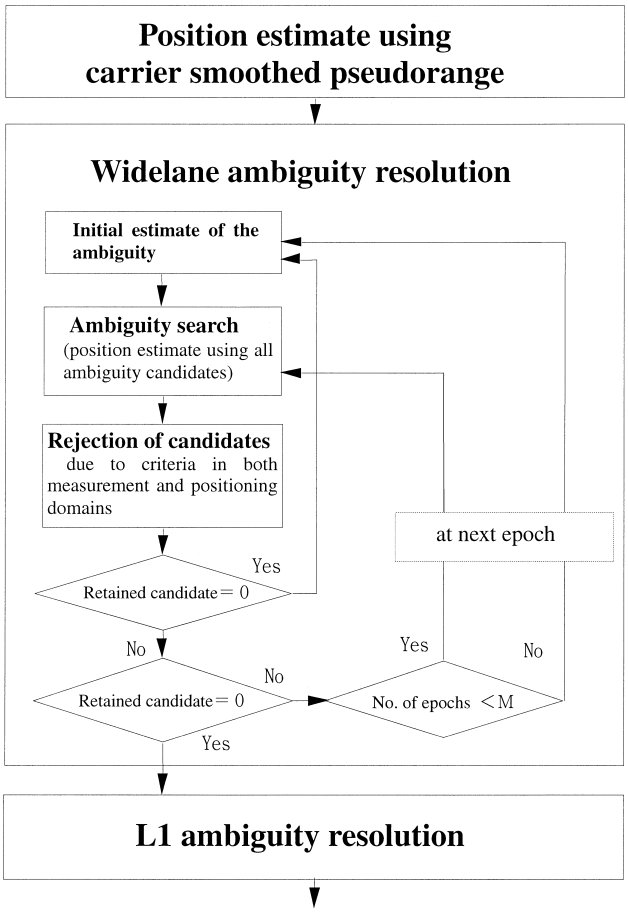

Figure 2-5 Flowchart of the OTF algorithm

$$\nabla\Delta N_{W0} = idnint\left(\frac{\nabla\Delta\phi_W - \nabla\Delta\rho^* - \nabla\Delta d_{trop}}{\lambda_W}\right) \tag{2.2-4}$$

The double differenced geometrical distances from the receiver to satellites, $\Delta\nabla\rho^*$, are calculated using pseudorange-position, and the tropospheric propagation delays are calculated using the Saastamoinen's zenith delay model with CfA2.2 mapping function (Chapter 3.1.2). The notation" $idnint$ "means to make nearest integer. The correct integer ambiguity should be in a domain centered to the initial value shown in the following equation:

$$\nabla\Delta N^i_{W0} - k\sigma^W_N \le \nabla\Delta N^i_W \le \nabla\Delta N^i_{W0} + k\sigma^W_N \quad (i = 1,2,\cdots,nsv-1) \tag{2.2-5}$$

where nsv denotes number of observed satellites, and σ^W_N denotes the standard deviation of initially estimated widelane ambiguity (see Figure 1-1). We set the integer k to 2 or 3, which correspond to the significant level of 95% or 99%, respectively. Although some authors developed new methods to reduce the search number[26)-28)], we search the whole cube for the simplicity of the algorithm.

Now, we choose four satellites that have the minimum RDOP (Relative Dilution of Precision) as primary satellites among all of the observed satellites. The RDOP is a factor that is defined by the distribution of observed satellites in the sky, and given by the following equations:

$$RDOP = \sqrt{trace(H^T H)^{-1}} \tag{2.2-6}$$

$$\mathbf{H} = \left(\frac{\partial DD_1}{\partial \mathbf{r}} \cdots \frac{\partial DD_{nsv-1}}{\partial \mathbf{r}}\right)^{\mathrm{T}} = \begin{pmatrix} \frac{\mathbf{r}^T - \mathbf{r}^{*T}_{SV1}}{\rho^{*1}_u} & - & \frac{\mathbf{r}^T - \mathbf{r}^{*T}_{SV2}}{\rho^{*2}_u} \\ & \vdots & \\ \frac{\mathbf{r}^T - \mathbf{r}^{*T}_{SV1}}{\rho^{*1}_u} & - & \frac{\mathbf{r}^T - \mathbf{r}^{*T}_{SVnsv}}{\rho^{*nsv}_u} \end{pmatrix} \tag{2.2-7}$$

where H is the measurement matrix. ρ^{*i}_u is the distance from user receiver to i-th satellite. DD_i is the double differenced observable between the first and i+1-th satellite, in which the smoothed pseudorange, widelane, or L1 carrier phase should be inserted. Using the RDOP, the standard deviation of double differenced measurement error σ_m and positioning error σ_p satisfy the following relation:

$$\sigma_P = RDOP \cdot \sigma_m \tag{2.2-8}$$

If three ambiguities of primary satellites are resolved, the position of the user receiver is obtained. Therefore, the ambiguities of secondary satellites can be computed by inserting the position calculated using ambiguities of primary satellites instead of the pseudorange-position into $\Delta\nabla\rho^*$ of the right side of Eq. (2.2-4). Therefore, we firstly resolve the ambiguities of primary satellites by the least squares searching method, and the ambiguities of the secondary satellites are resolved next. The covariance matrix of widelane ambiguity estimated using Eq. (2.2-4) is given by the following equation:

$$C^W_N = H(H^T C^{-1}_{PR} H)^{-1} H^T + C_W \tag{2.2-9}$$

where C_{PR} and C_W are the measurement error covariance matrix of smoothed pseudorange and widelane. When four primary satellites are used for positioning, there exists the inverse matrix, H^{-1}. Eq. (2.2-9) is then simplified as

$$C^W_N = C_{PR} + C_W \tag{2.2-10}$$

Hence, the standard deviation of the initially estimated ambiguity σ_N^W is

$$\sigma_N^W = \sqrt{\sigma_m^{PR2} + \sigma_m^{W2}} \cong 65cm \tag{2.2-11}$$

where $\sigma_m^{PR} = \sqrt{E\{(\Delta\nabla\varepsilon_{PR})^2\}}$ and $\sigma_m^W = \sqrt{E\{(\Delta\nabla\varepsilon_W)^2\}}$ are the standard deviations of smoothed pseudorange and widelane measurements, and the value right side is for a Trimble 4000SSE receiver. Figure 2-6 shows the relationship between the initial value of ambiguity and the candidate of ambiguity solution. Since the wavelength of widelane is about 86cm, the solution is in a range of initial value ± 2 cycles with a significant level of 99%. Assuming that a range of initial value ± j cycles is to be searched, the number of ambiguity candidate becomes $(2j+1)^3$. In this case, the search number is 5^3=125.

(2) Receiver position is computed with each ambiguity candidate, and the statistical tests are performed in the measurement domain and positioning domain.

(2a) Test in the measurement domain

The χ^2 test is performed using the sum of measurement residuals. The candidates satisfying the following condition are rejected:

$$\frac{\upsilon^T C_W^{-1} \upsilon}{df} > \frac{\chi^2_{df,1-\alpha}}{df} k_1^W \tag{2.2-12}$$

where υ, α, and df denote the residual vector, the significant level of the χ^2 test, and the degree of freedom (= nsv-1), respectively. k_1^W is an empirical parameter of tolerance, which is set to 1～2 in the experiments considered in this paper.

(2b) Test in the positioning domain

Taking the differences between the horizontal position computed using smoothed pseudorange and those using each ambiguity candidate, the candidates satisfy the following condition are rejected:

$$|\mathbf{r}^{PR} - \mathbf{r}^W|_H > k_2^W \sigma_H^{PR-W} \tag{2.2-13}$$

where $\mathbf{r}^{PR}$ and $\mathbf{r}^W$ denote the position vectors of antenna calculated using smoothed pseudorange and wide lane, respectively, and $|\cdot|_H$ means to take the horizontal norm σ_H^{PR-W} shows the standard deviation of the difference between the pseudorange-position and the widelane-position in the horizontal direction. k_2^W is an empirical parameter of tolerance, which is set to 2 or 3 in the experiments considered in this paper. Theoretically, $k_2^W = 1,\ 2,\ 3$ corresponds to the significant level of 68, 95, and 99%.

The standard deviation of position error when the pseudoranges are used is written as follows

$$\sigma_p^{PR} = RDOP \cdot \sigma_m^{PR} \tag{2.2-14}$$

where σ_m^{PR} is the standard deviation of pseudorange measurement error. This equation can be divided into horizontal

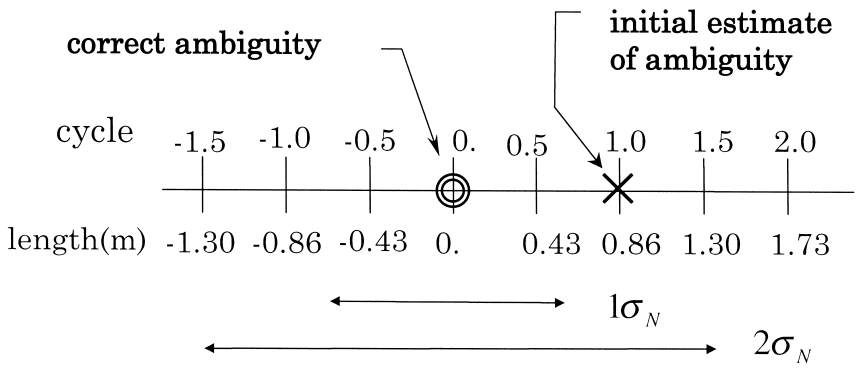

Figure 2-6 Relationship among the correct ambiguity, initial estimate of ambiguity, and its error

and vertical directions:

$$\begin{aligned}\sigma_H^{PR} &= RHDOP \cdot \sigma_m^{PR} \\ \sigma_V^{PR} &= RVDOP \cdot \sigma_m^{PR} \\ RDOP &= \sqrt{RHDOP^2 + RVDOP^2}\end{aligned} \tag{2.2-15}$$

The $RHDOP$ and $VDOP$ indicate the dilution of relative positioning precision in the horizontal and vertical directions. The standard deviation of positioning error for widelane is written in a similar form. Therefore, the standard deviation of the difference between the pseudorange-position and widelane-position is given as follows

$$\sigma_H^{PR-W} = RHDOP\sqrt{\sigma_m^{PR2} + \sigma_m^{W2}} \tag{2.2-16}$$

If the considered ambiguity candidate is correct, the standard deviation will be

$$\sigma_H^{PR-W} = RHDOP\sqrt{65^2 + 4^2} \cong 65 \cdot RHDOP \ (cm) \tag{2.2-17}$$

However, if there are 1-cycle errors, for example, in each ambiguity, the difference between the pseudorange-position and widelane-position will be increased as follows

$$|\mathbf{r}^{PR} - \mathbf{r}^{W}|_H \cong RHDOP\sqrt{65^2 + 86^2} \cong 108 \cdot RHDOP \ (cm) \tag{2.2-18}$$

Therefore, the candidate may be rejected according to Inequality (2.2-13).

Although the horizontal position difference is evaluated in the above equations, the same result will be expected theoretically even if the vertical or three dimensional position difference is evaluated. The expectation is based on the assumption that the measurement errors are gaussian noises. However in reality, it is very difficult to completely remove the systematic errors from the measurements by theoretical models or by taking the double difference. The unremoved errors are propagation delay, ephemeris error, and multipath error, which degrade mainly the vertical positioning accuracy. Namely, since the vertical position scatters widely due to the unremoved errors, the usage of vertical position for the test causes an increase in the number of candidates that cannot be rejected. Therefore, it is better to evaluate the horizontal position in the positioning domain test.

(3) If one ambiguity candidate set is retained, that is considered as the solution. And if more than one candidate are retained, similar statistical tests will be performed at the next epoch.

The tests shown in Eq. (2.2-12,13) are called local tests because measurement data of a single epoch are used. In addition to the local tests, the global tests that use the data of multiple epochs are performed.

(4) Procedure (2) and (3) are repeated until only one candidate is retained. If the number of total epochs exceed a threshold number, M, the process is back to (1).

(5) The initial values of L1 ambiguity are calculated from the widelane-position.

The standard deviation of initially estimated L1 ambiguity, σ_N^{L1}, is calculated by a similar equation with (2.2-11) as follows

$$\sigma_N^{L1} = \sqrt{\sigma_m^{W2} + \sigma_m^{L12}} \cong 4cm \tag{2.2-19}$$

Since the L1 wavelength is 19cm, the solution will be in a range of initial ambiguity $\pm$ 1 cycle (99%), and the search number is $3^3 = 27$.

(6) Procedures similar to (2) and (3) are repeated until only one candidate is retained. If the number of total epochs exceed a threshold number, M, the process is back to (5).

In the case of L1 ambiguity resolution, the test in positioning domain is very powerful. The standard deviation of the difference between the widelane-position and the L1-position is given by the next equation

$$\sigma_H^{W-L1} = RHDOP\sqrt{\sigma_m^{W2} + \sigma_m^{L12}} \tag{2.2-20}$$

If the ambiguities are correct, it will be

$$\sigma_H^{W-L1} = RHDOP\sqrt{4^2 + 1^2} \cong 4 \cdot RHDOP \ \ (cm) \tag{2.2-21}$$

However, if the ambiguities are with 1-cycle errors, it will be approximately

$$|\mathbf{r}^W - \mathbf{r}^{L1}|_H \cong RHDOP\sqrt{4^2 + 19^2} \cong 19.4 \cdot RHDOP \ \ (cm) \tag{2.2-22}$$

Therefore, the considered candidate can be rejected easily. In Eq. (2.2-22), the horizontal position difference is evaluated as well as in the case of widelane ambiguity resolution.

There are two advantages in our OTF algorithm as follows:

A) The number of ambiguity candidate sets can be reduced effectively by resolving the widelane ambiguity before resolving the L1 ambiguity.

In our experimental configuration, the number of ambiguity candidates with a significant level of 99% are 125 and 27 for widelane and L1 ambiguity resolution, respectively; therefore, the total number of searches is 125+27=152. On the other hand, if we resolve the L1 ambiguity set directly from the pseudorange-position, the number of searches can be calculated from the equations below,

$$\sigma_N^{L1} = \sqrt{\sigma_m^{PR2} + \sigma_m^{L12}} \cong 65cm, \quad \frac{3\sigma_N^{L1}}{\lambda_1} - \cong 10\,cycle \tag{2.2-23}$$

namely, $(2 \times 10 + 1)^3 = 9261$, which is approximately 60 times as large as in the former case.

B) The ambiguity of the L1 carrier phase is resolved quickly and reliably by conducting the test in the positioning domain, which can be adopted if the widelane observable is used intermediately.

Assuming that the widelane observable is not used, the standard deviation of the difference between the pseudorange-position and the L1-position will become as follows when the ambiguities are correct:

$$\begin{aligned} \sigma_H^{PR-L1} &= RHDOP\sqrt{\sigma_m^{PR2} + \sigma_m^{L12}} \\ &= RHDOP\sqrt{65^2 + 1^2} \cong 65 \cdot RHDOP \ \ (cm) \end{aligned} \tag{2.2-24}$$

Also, when the ambiguities are with 1-cycle errors, the position difference will be

$$|\mathbf{r}^{PR} - \mathbf{r}^{L1}|_H \cong RHDOP\sqrt{65^2 + 19^2} \cong 68 \cdot RHDOP \ \ (cm) \tag{2.2-25}$$

which is not so different from the former case. This means the statistical test in the positioning domain has no effect in this case.

2. 3 Cycle Slip Detection

The cycle slip occurs if the receiver loses phase lock of the satellite signal. The most frequent reason is signal obstruction due to trees, buildings, or vehicles themselves. Another reason is a low SNR due to bad ionospheric conditions, multipath, high receiver dynamics, or low satellite elevation. When a cycle slip occurs, the carrier phase jumps by an integer cycle while the fractional part of the phase remains unchanged. The cycle slip may be as small as a few cycles, or exceed millions of cycles. Cycle slips have to be detected because the corresponding measurements are not available for positioning until the new ambiguities are resolved. However, cycle slips can be easily detected for dual frequency by monitoring the ionospheric signal in Eq. (2.1-30). Taking the time difference of the ionospheric signal and denoting it, $SLIP$, the result with no cycle slip is

$$\begin{aligned} SLIP &\equiv \Phi_1(t_n) - \Phi_1(t_{n-1}) \\ &= -2\{I(t_n) - I(t_{n-1})\} \end{aligned} \tag{2.3-1}$$

where the multipath and measurement noise are omitted. If a cycle slip occurs in the L1 and L2 carriers as δN_1 and δN_2, the index will jump as

$$\begin{aligned} SLIP &= -2\{I(t_n) - I(t_{n-1})\} + \lambda_N(\delta N_1 + \delta N_2) - \lambda_W(\delta N_1 - \delta N_2) \\ &= -2\{I(t_n) - I(t_{n-1})\} - 75.5 \cdot \delta N_1 + 96.9 \cdot \delta N_2 \quad (cm) \end{aligned} \tag{2.3-2}$$

Assuming the measurement noise of L1 and L2 carrier phase as 0.1 radians, corresponding to 3mm and 3.9mm, respectively, the measurement noise of the ionospheric signal is 20mm. Then the measurement noise in SLIP becomes 28mm because the time difference is taken. Therefore, even a cycle slip of one cycle in the L1 or L2 carrier would be easily detected by using a threshold value, 8.4cm (3σ). However, there are some special cases in which the detection is very difficult, for example, 5-cycles slip in the L1 and 4-cycles in the L2 carrier, that cause only a 10cm jump in $SLIP$. Nevertheless, since L1 and L2 cycle slips are independent and normally large numbers, we adopt this index to detect cycle slips. When a cycle slip is detected and the phase locks of more than three satellites are maintained, the corresponding ambiguity is computed using the receiver position obtained from the remaining satellites' carrier phases. And if the number of satellites maintaining the phase locks becomes less than four, the OTF is performed as the initialization. Instead of the initialization, some methods of cycle slip fixing have been proposed using a simple linear regression[21], or using the Kalman filtering[29), 30)].

If L1 single frequency receiver is used, the cycle slip may be detected using the carrier smoothed pseudorange[9], $\bar{PR}_1$, as

$$\begin{aligned} SLIP_S &\equiv \{\Phi_1(t_n) - \bar{PR}_1(t_n)\} - \{\Phi_1(t_{n-1}) - \bar{PR}_1(t_{n-1})\} \\ &= -2\frac{f_2}{f_1}\{I(t_n) - I(t_{n-1})\} \end{aligned} \tag{2.3-3}$$

or using the carrier doppler, $\dot{\Phi}_1$, as

$$SLIP_D \equiv \{\Phi_1(t_n) - \Phi_1(t_{n-1})\} - \dot{\Phi}_1(t_n) \cdot (t_n - t_{n-1}) \tag{2.3-4}$$

However, the detection of a few cycles slip would be difficult because the accuracy of smoothed pseudorange is normally worse than 50cm and the doppler changes significantly during the observation interval. If the smoothed pseudorange or carrier doppler were sufficiently accurate, these indexes could be used for cycle slip fixing.

2. 4 Positioning Algorithm

Two types of positioning methods are used in our software. The least squares method is used in the OTF algorithm to calculate positions for each ambiguity candidate set. And the extended Kalman filter is used for positioning after the widelane/L1 ambiguity are resolved, while the least squares method is also available in this case. Since the accuracy of position estimated by the extended Kalman filter depends on the aircraft dynamics, it would degrade during the strong maneuvers.

2. 4. 1 Least Squares Method

Herein, the double differenced measurement vector is denoted by $\mathbf{y}$ as

$$\mathbf{y} = (DD_1, DD_2, \cdots DD_{nsv-1})^T \tag{2.4-1}$$

where DD is the double difference of pseudorange, widelane, or L1 carrier phase.

Denoting a priori position of the receiver by $\bar{\mathbf{r}}$, and computed measurement vector by $\bar{\mathbf{y}}$, the next relation is satisfied

$$\begin{aligned}\mathbf{y}-\bar{\mathbf{y}}&=H(\mathbf{r}-\bar{\mathbf{r}})+\mathbf{e}\\ \delta\mathbf{y}&=H\delta\mathbf{r}+\mathbf{e}\end{aligned} \tag{2.4-2}$$

where H and $\mathbf{e}$ are the measurement matrix written in Eq. (2.2-7) and the measurement error vector. We wish to minimize the scalar cost function J, where

$$J=(\delta\mathbf{y}-H\delta\mathbf{r})^T C^{-1}(\delta\mathbf{y}-H\delta\mathbf{r}) \tag{2.4-3}$$

C is the covariance matrix of the measurement given as

$$\begin{aligned}C&=E[\mathbf{e}\mathbf{e}^T]\\ &=E[(\boldsymbol{\varepsilon}_1^1-\boldsymbol{\varepsilon}_1^2-\boldsymbol{\varepsilon}_2^1+\boldsymbol{\varepsilon}_2^2, \boldsymbol{\varepsilon}_1^1-\boldsymbol{\varepsilon}_1^3-\boldsymbol{\varepsilon}_2^1+\boldsymbol{\varepsilon}_2^3, \cdots, \boldsymbol{\varepsilon}_1^1-\boldsymbol{\varepsilon}_1^{nsv}-\boldsymbol{\varepsilon}_2^1+\boldsymbol{\varepsilon}_2^{nsv})^T\\ &\quad (\boldsymbol{\varepsilon}_1^1-\boldsymbol{\varepsilon}_1^2-\boldsymbol{\varepsilon}_2^1+\boldsymbol{\varepsilon}_2^2, \boldsymbol{\varepsilon}_1^1-\boldsymbol{\varepsilon}_1^3-\boldsymbol{\varepsilon}_2^1+\boldsymbol{\varepsilon}_2^3, \cdots, \boldsymbol{\varepsilon}_1^1-\boldsymbol{\varepsilon}_1^{nsv}-\boldsymbol{\varepsilon}_2^1+\boldsymbol{\varepsilon}_2^{nsv})]\\ &=2s^2\begin{pmatrix}2 & & 1\\ & \ddots & \\ 1 & & 2\end{pmatrix}\end{aligned} \tag{2.4-4}$$

assuming that the measurement errors are independent for all satellites and the standard deviations are the same which is denoted by $s(=\sqrt{E[\boldsymbol{\varepsilon}^2]})$. The superscript of $\boldsymbol{\varepsilon}$ denotes the satellite number and the subscript denotes the receiver number, not the L1/L2 band. Then the inverse of covariance is given as follows

$$C^{-1}=\frac{1}{nsv}\frac{2}{s^2}\begin{pmatrix}\mathrm{nsv}-1 & & -1\\ & \ddots & \\ -1 & & \mathrm{nsv}-1\end{pmatrix} \tag{2.4-5}$$

The weighted least squares estimate is then given as

$$\delta\mathbf{r}=(H^T C^{-1}H)^{-1}H^T C^{-1}\delta\mathbf{y} \tag{2.4-6}$$

If the measurement error, $\mathbf{e}$, is assumed to be a zero mean and gaussian-distributed noise, the estimate is also the maximum likelihood estimate. In our software, an orthogonal transformation approach with the givens rotation is used as follows:

$$\mathbf{U}\delta\mathbf{r}=\mathbf{b} \tag{2.4-7}$$

where $\mathbf{U}$ is the upper triangular matrix and the estimate is obtained by backward substitution.

The error covariance matrix of the state is given as

$$C_{\mathbf{r}}=(H^T C^{-1}H)^{-1} \tag{2.4-8}$$

Denting the diagonal elements of $C_{\mathbf{r}}$ by q_{xx}, q_{yy}, q_{zz}, the standard deviation of position estimate, $\boldsymbol{\sigma}_p$, is

$$\begin{aligned}\boldsymbol{\sigma}_p&=\sqrt{q_{xx}+q_{yy}+q_{zz}}\\ &=\sqrt{trace(H^T C^{-1}H)^{-1}}\end{aligned} \tag{2.4-9}$$

Here, we define the $RDOP$ as

$$RDOP\equiv\sqrt{trace(H^T C^{-1}H)/\boldsymbol{\sigma}_m^2} \tag{2.4-10}$$

where σ_m^2 is the standard deviation of double differenced measurement that is equal to the diagonal element of C, i.e., $4s^2$ (in the OTF algorithm, $RDOP$ is simplified as Eq. (2.2-6)). Therefore, the standard deviation of position and measurement satisfy Eq. (2.2-8),

$$\sigma_p = RDOP \cdot \sigma_m \tag{2.2-8}$$

If the carrier doppler data are available, the velocity of user receiver is estimated more precisely. Since the carrier doppler is time derivative of the carrier phase, the observation equation and its double difference are expressed as follows

$$\dot{\phi} = \dot{\rho}^* - \frac{f_2}{f_1}\dot{I} + \dot{d}_{trop} + \dot{b} - \dot{b}_{SV} + \dot{d}_{eph} + \dot{d}_{m,phase} + \dot{\varepsilon} \tag{2.4-11}$$

$$\nabla\Delta\dot{\phi} = \nabla\Delta\dot{\rho}^* + \nabla\Delta\dot{\varepsilon} \tag{2.4-12}$$

In Eq. (2.4-12), most of the measurement errors are neglected. When the velocity is estimated, the measurement matrix, H, is extended as follows

$$H = \left(\frac{\partial \nabla\Delta\phi_1}{\partial \mathbf{r}} \cdots \frac{\partial \nabla\Delta\phi_{nsv-1}}{\partial \mathbf{r}} \quad \frac{\partial \nabla\Delta\dot{\phi}_1}{\partial \dot{\mathbf{r}}} \cdots \frac{\partial \nabla\Delta\dot{\phi}_{nsv-1}}{\partial \dot{\mathbf{r}}} \right)^T$$

$$= \begin{pmatrix} \frac{\mathbf{r}^T - \mathbf{r}_{SV1}^{*T}}{\rho_u^{*1}} - \frac{\mathbf{r}^T - \mathbf{r}_{SV2}^{*T}}{\rho_u^{*2}} & & O_{(nsv-1)\times 3} \\ \vdots & & \\ \frac{\mathbf{r}^T - \mathbf{r}_{SV1}^{*T}}{\rho_u^{*1}} - \frac{\mathbf{r}^T - \mathbf{r}_{SV nsv}^{*T}}{\rho_u^{*nsv}} & & \\ \frac{\dot{\mathbf{r}}^T - \dot{\mathbf{r}}_{SV1}^{*T}}{\rho_u^{*1}} - \frac{\dot{\mathbf{r}}^T - \dot{\mathbf{r}}_{SV2}^{*T}}{\rho_u^{*2}} & \frac{\mathbf{r}^T - \mathbf{r}_{SV1}^{*T}}{\rho_u^{*1}} - \frac{\mathbf{r}^T - \mathbf{r}_{SV2}^{*T}}{\rho_u^{*2}} \\ \vdots & \vdots \\ \frac{\dot{\mathbf{r}}^T - \dot{\mathbf{r}}_{SV1}^{*T}}{\rho_u^{*1}} - \frac{\dot{\mathbf{r}}^T - \dot{\mathbf{r}}_{SV nsv}^{*T}}{\rho_u^{*nsv}} & \frac{\mathbf{r}^T - \mathbf{r}_{SV1}^{*T}}{\rho_u^{*1}} - \frac{\mathbf{r}^T - \mathbf{r}_{SV nsv}^{*T}}{\rho_u^{*nsv}} \end{pmatrix} \tag{2.4-13}$$

And the error covariance matrix of the measurement and the state, (C, C_x) are also extended correspondingly.

2. 4. 2 Extended Kalman Filter

A system dynamics below is considered in the Kalman filtering.

$$\dot{\mathbf{x}} = F\mathbf{x} + B\mathbf{u} \tag{2.4-14}$$

In our application, the state vector contains the aircraft position, velocity and acceleration ($\mathbf{r}$, $\mathbf{v}$, $\mathbf{a}$) as follows

$$\mathbf{x} = \begin{pmatrix} \mathbf{r} \\ \mathbf{v} \\ \mathbf{a} \end{pmatrix} \tag{2.4-15}$$

The so-called acceleration dead reckoning (ADR) model is adopted as an aircraft dynamics model:

$$\begin{cases} \dot{\mathbf{r}} = \mathbf{v} \\ \dot{\mathbf{v}} = \mathbf{a} \\ \dot{\mathbf{a}} = -\frac{1}{\tau}\mathbf{a} + \mathbf{u} \end{cases} \tag{2.4-16}$$

Namely, a Gauss-Markov process is assumed for acceleration, in which τ is the time constant and $\mathbf{u}$ is the white noise. This can be written in the next form,

$$\begin{pmatrix} \dot{\mathbf{r}} \\ \dot{\mathbf{v}} \\ \dot{\mathbf{a}} \end{pmatrix} = \begin{pmatrix} O_{3\times3} & I_{3\times3} & O_{3\times3} \\ O_{3\times3} & O_{3\times3} & I_{3\times3} \\ O_{3\times3} & O_{3\times3} & -\frac{1}{\boldsymbol{\tau}} I_{3\times3} \end{pmatrix} \begin{pmatrix} \mathbf{r} \\ \mathbf{v} \\ \mathbf{a} \end{pmatrix} + \begin{pmatrix} O_{3\times3} \\ O_{3\times3} \\ I_{3\times3} \end{pmatrix} \mathbf{u} \tag{2.4-17}$$

Then, the matrix F and B are expressed as

$$F = \begin{pmatrix} O_{3\times3} & I_{3\times3} & O_{3\times3} \\ O_{3\times3} & O_{3\times3} & I_{3\times3} \\ O_{3\times3} & O_{3\times3} & -\frac{1}{\boldsymbol{\tau}} I_{3\times3} \end{pmatrix}, \quad B = \begin{pmatrix} O_{3\times3} \\ O_{3\times3} \\ I_{3\times3} \end{pmatrix} \tag{2.4-18}$$

The covariance matrix for the process noise $\mathbf{u}$ is given by

$$Q = E\{\mathbf{u}\mathbf{u}^T\} = \begin{pmatrix} q_{ax} & 0 & 0 \\ 0 & q_{ay} & 0 \\ 0 & 0 & q_{az} \end{pmatrix} \tag{2.4-19}$$

In order to implement this system model into the computer programs, the differential equation of motion has to be transformed to a discrete form such as

$$\mathbf{x}(t_k) = \boldsymbol{\Phi}(t_k, t_{k-1})\mathbf{x}(t_{k-1}) + G(t_k)\mathbf{w}(t_k) \tag{2.4-20}$$

where

$$E\{\mathbf{w}(t_k)\mathbf{w}(t_l)^T\} = Q'(t_k) \cdot \boldsymbol{\delta}_{kl} \tag{2.4-21}$$

This form is also suited for the U-D factorization in which the numerical stability is of special concern[31]. Then the problem herein is to express matrixes $\boldsymbol{\Phi}$, G, Q' by F, B, Q.

The matrix $\boldsymbol{\Phi}$ and F generally satisfy the following equations

$$\dot{\boldsymbol{\Phi}}(t, t_{k-1}) = F(t)\boldsymbol{\Phi}(t, t_{k-1}) \tag{2.4-22}$$

$$\boldsymbol{\Phi}(t_{k-1}, t_{k-1}) = I \tag{2.4-23}$$

Since the matrix $F(t)$ is constant ($=F$) in this application, the state transition matrix $\boldsymbol{\Phi}$ is expressed by F as the next equation

$$\begin{aligned} \boldsymbol{\Phi}(t, t_{k-1}) &= \boldsymbol{\Phi}(t - t_{k-1}) \\ &= e^{F \cdot (t - t_{k-1})} \\ &= I + F \cdot (t - t_{k-1}) + \frac{1}{2!} F^2 \cdot (t - t_{k-1})^2 + \cdots \end{aligned} \tag{2.4-24}$$

Therefore, the transition matrix is given explicitly as follows

$$\begin{aligned} \boldsymbol{\Phi}(t_k, t_{k-1}) &= \boldsymbol{\Phi}(\boldsymbol{\Delta}) \\ &= \begin{pmatrix} I_{3\times3} & \boldsymbol{\Delta} I_{3\times3} & \boldsymbol{\Phi}_{13} \\ O_{3\times3} & I_{3\times3} & \boldsymbol{\Phi}_{23} \\ O_{3\times3} & O_{3\times3} & \boldsymbol{\Phi}_{33} \end{pmatrix} \end{aligned} \tag{2.4-25}$$

$$\begin{aligned}\Phi_{13}&=\frac{\Delta^2}{2}-\frac{\Delta^3}{6\tau}\\ \Phi_{23}&=\Delta-\frac{\Delta^2}{2\tau}+\frac{\Delta^3}{6\tau^2}\\ \Phi_{33}&=1-\frac{\Delta}{\tau}+\frac{\Delta^2}{2\tau^2}-\frac{\Delta^3}{6\tau^3}\end{aligned} \tag{2.4-26}$$

where the fourth or higher order terms concerning $\Delta(=t_k-t_{k-1})$ are neglected. On the other hand, the solution of Eq. (2.4-14) is given by

$$\mathbf{x}(t_k)=\Phi(t_k,\ t_{k-1})\mathbf{x}(t_{k-1})+\int_{t_{k-1}}^{t_k}\Phi(t_k,\xi)B(\xi)\mathbf{u}(\xi)d\xi \tag{2.4-27}$$

The second part of the right side,

$$\mathbf{x}'\equiv\int_{t_{k-1}}^{t_k}\Phi(t_k,\xi)B(\xi)\mathbf{u}(\xi)d\xi \tag{2.4-28}$$

is the accumulated process noise between t_{k-1} and t_k. If the process noise $\mathbf{u}$ were constant from t_{k-1} to t_k as $\mathbf{u}'(t_k)$, Eq. (2.4-27) would be approximated as

$$\mathbf{x}'\cong\left[\int_{t_{k-1}}^{t_k}\Phi(t_k,\xi)B(\xi)d\xi\right]\cdot\mathbf{u}'(t_k) \tag{2.4-29}$$

Comparing this with Eq. (2.4-20), G and w will be of the form:

$$\begin{aligned}G(t_k)&=\int_{t_{k-1}}^{t_k}\Phi(t_k,\xi)Bd\xi\\ &=\begin{pmatrix}\frac{\Delta^3}{6}I_{3\times3}\\ \left(\frac{\Delta^2}{2}-\frac{\Delta^3}{6\tau}\right)I_{3\times3}\\ \left(\Delta-\frac{\Delta^2}{2\tau}+\frac{\Delta^3}{6\tau^2}\right)I_{3\times3}\end{pmatrix}\end{aligned} \tag{2.4-30}$$

$$\mathbf{w}(t_k)\equiv\mathbf{u}'(t_k) \tag{2.4-31}$$

Now, we adopt an average of process noise as $\mathbf{u}'(t_k)$, i.e.,

$$\mathbf{u}'(t_k)\equiv\int_{t_{k-1}}^{t_k}\mathbf{u}(\xi)d\xi/\Delta \tag{2.4-32}$$

Then the covariance for process noise in the discrete model will be

$$\begin{aligned}Q'(t_k)&=E\left(\mathbf{u}'(t_k)\mathbf{u}'(t_k)^T\right)\\ &=\int_{t_{k-1}}^{t_k}Q(\xi)d\xi/\Delta^2\end{aligned} \tag{2.4-33}$$

Since the covariance for process noise is assumed to be constant in this model as $Q(\xi)=Q$, it will be

$$\begin{aligned}Q'&=Q/\Delta\\ &=\begin{pmatrix}q_{ax}/\Delta & 0 & 0\\ 0 & q_{ay}/\Delta & 0\\ 0 & 0 & q_{az}/\Delta\end{pmatrix}\end{aligned} \tag{2.4-34}$$

On the other hand, the measurement equations, which are already given by Eq. (2.2-1,2,3), can be written as

$$\mathbf{y}=h(\mathbf{x})+\mathbf{e} \tag{2.4-35}$$

The measurement matrix $H=\left(\frac{\partial h}{\partial \mathbf{x}}\right)^T$ and the error covariance for measurement are given in Eq. (2.2-7) and Eq. (2.4-4). If the velocity of the user receiver would be estimated, the extended measurement matrix (Eq. (2.4-13)) and the covariance matrix would be used. Though the measurements are given in the form of vector, they are treated as an order of scalar in the computer program. Now we gave the entire matrixes requisite for implementation of the extended Kalman filter.

3. Evaluation of Positioning Accuracy

Although several efforts have been made in order to evaluate the positioning accuracy by KGPS, it is difficult to find other equipment for positioning whose accuracy is similar or better than KGPS. A laser tracker can be imagined, but there seem to be some problems. For example, it is difficult to calibrate the tracker mounting error with sufficient accuracy, and its positioning accuracy degrades when the distance between the tracker and the reflector is increased. An attempt will be made here, namely, analyses of static baselines by KGPS. Solutions of KGPS will be compared with the positions which were determined previously by software for static survey, and the time variation of positioning error and effects of various errors will be discussed. Data taken from the Izu-Islands area are used for the evaluation. Since this area is located in a volcanically and tectonically active zone, a number of GPS receivers have been installed by several organizations. We analyzed eight baselines with various lengths chosen from six observation sites. Then the possibility of OTF depending on the baseline length is discussed using the same data. Finally, we demonstrate that a crustal movement due to an earthquake with a few centimeters level can be detected by kinematic GPS positioning[32].

3. 1 Evaluation of Positioning Accuracy Using Static Data

3. 1. 1 Comparison with Static Positioning Solutions

We analyzed data from six observation sites, namely Kozujima, Niijima, Miyakeizu, Miyaketsubota, Minamiizu, and Shizuoka. Locations of those sites are shown in Figure 3-1, The eight baselines used and their lengths are listed in Table 3-1. The receivers are Trimble 4000SSE, and those antennas are with groundplanes that mitigate the multipath effect. Data from Minamiizu are provided by the University of Tokyo, and others are by the Geodetic Survey Institute of Japan.

An earthquake with magnitude 5.6 occurred on 6 Oct. 1995, in the sea near Kozujima, and accordingly the position of Kozujima moved eastward 2-3 cm[33]. In order to compare the KGPS solutions with static position, we analyzed the data of 5 Oct. 1995 in this section. We assume that there was no crustal movement before the earthquake. Static position solutions of those sites were estimated by using the software, GAMIT, which was published at the Massachusetts Institute of Technology. The data were recorded from 6 to 18 o'clock in GPS time at 60-second intervals, and the precise ephemeris made by the International GPS Service (IGS) was used. Minamiizu site was used as a reference site, and positions of other sites were estimated relative to the reference site.

Then we compared the KGPS solution with the GAMIT solutions. Figure 3-2 (a-f) show the difference between these two solutions. In the kinematic analyses, double differenced ionospheric-free measurements were used, and the IGS precise ephemeris was also used instead of the broadcast ephemeris. The tropospheric propagation delay was calculated using the Saastamoinen's zenith delay model and the Cfa2.2 mapping function, where meteorological data were set to the standard values (temperature 20°C, humidity 50%, pressure 1013HPa) for all sites. In case of baselines No.1 - 5, L1 and L2 ambiguities

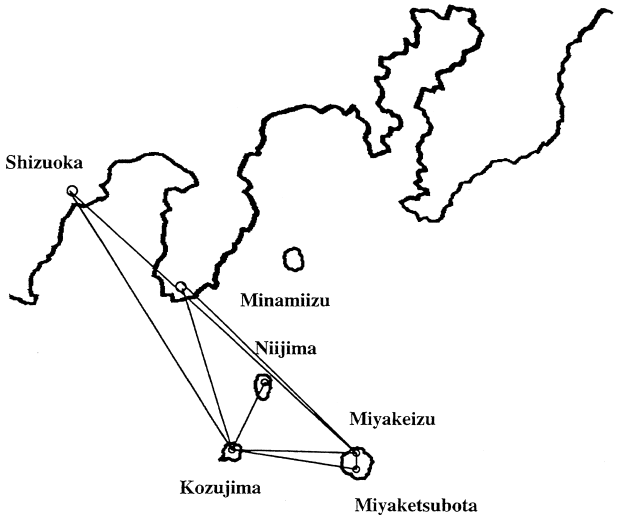

Figure 3-1 Map of Izu-Islands area

Table 3-1 Summery of baselines and their lengths

Baseline No.	Reference station	User station	baseline length(km)
1	Miyakeizu	Miyaketsubota	7.951
2	Niijima	Kouzujima	22.146
3	Miyakeizu	Kozujima	35.182
4	Miyaketsubota	Kozujima	41.173
5	Minamiizu	Kozujima	56.695
6	Minamiizu	Miyakeizu	84.029
7	Shizuoka	Kozujima	106.719
8	Shizuoka	Miyakeizu	136.005

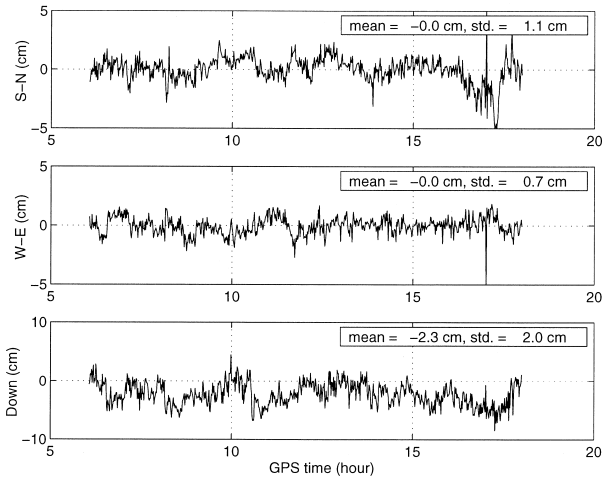

Figure 3-2a KGPS positioning errors when ionospheric-free observable was used (Miyakeizu - Miyaketsubota, 7.951km)

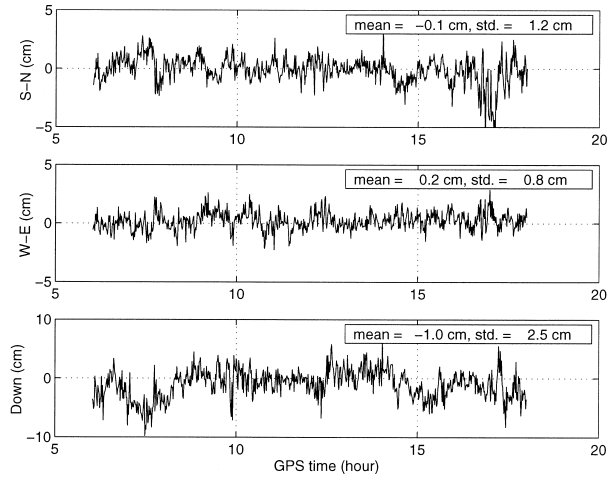

Figure 3-2b Errors of ionospheric-free KGPS solution (Niijima - Kozujima, 22.146km)

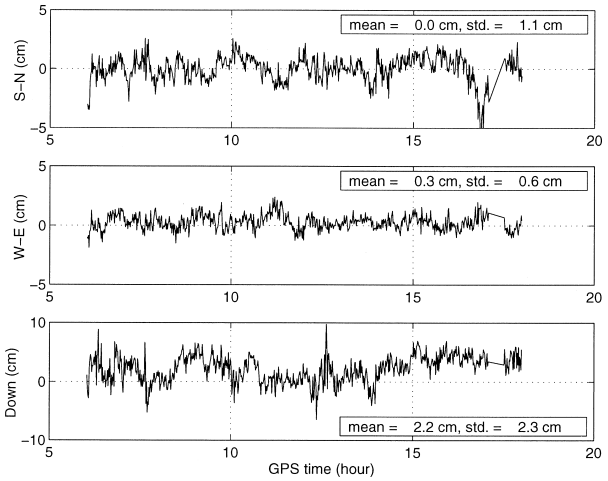

Figure 3-2c Errors of ionospheric-free KGPS solution (Miyakeizu - Kozujima, 35.182km)

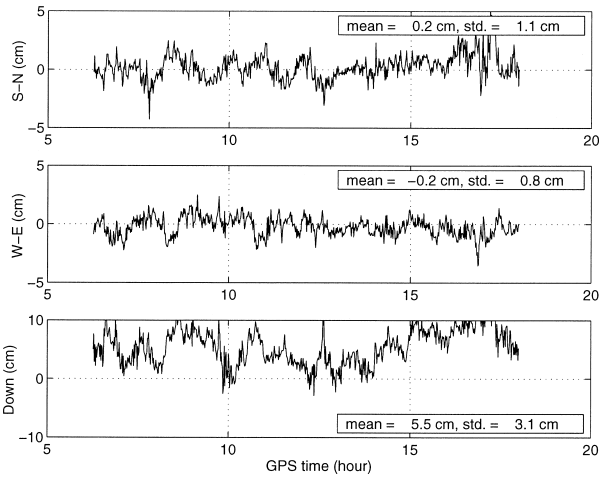

Figure 3-2d Errors of ionospheric-free KGPS solution (Miyaketsubota - Kozujima, 41.173km)

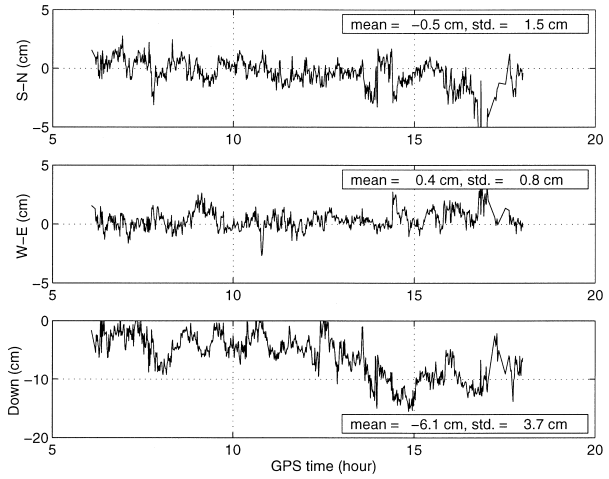

Figure 3-2e Errors of ionospheric-free KGPS solution (Minamiizu - Kozujima, 56.695km)

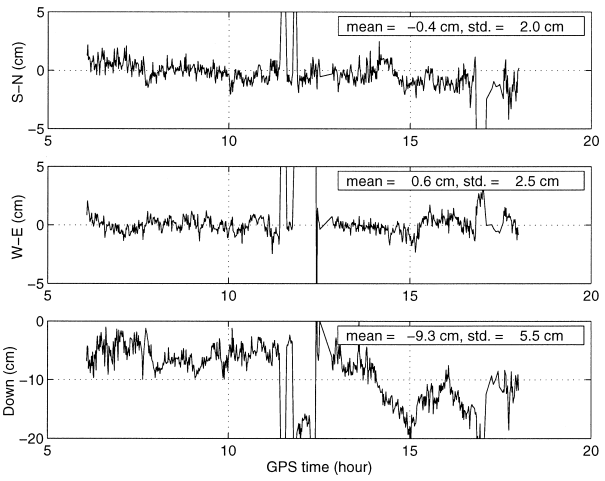

Figure 3-2f Errors of ionospheric-free KGPS solution (Minamiizu - Miyakeizu, 84.029km)

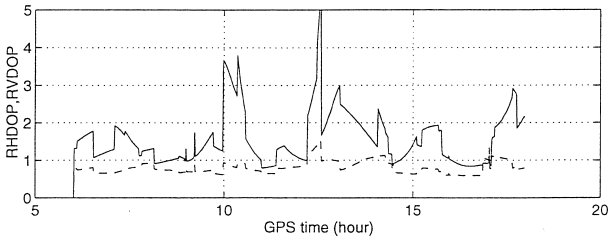

Figure 3-3 Variation of RHDOP and RVDOP
(Dashed line is RHDOP and solid line is RVDOP)

were correctly resolved except for a period around 17 o'clock and later. These miss-fixings of ambiguity occurred because only 4 to 5 satellites were visible and their constellation was inadequate in that period. Figure 3-3 shows the time variation of RHDOP and RVDOP for baseline No.2. The DOP values were quite similar for other baselines because we treated a local area. The RMS (Root Mean Square) of RHDOP and RVDOP during all observation time were 1.35 and 1.78 respectively. It can be seen clearly that the positioning accuracy correlates with the baseline length. For baseline No. 6, ambiguities were not resolved correctly from 11:30 to 12:30, and for baselines No.7 and 8, correct ambiguities were never resolved. Since the positioning accuracy obviously degrades according to the increase of baseline length, the baseline dependence of the various kinds of errors will be evaluated in the next section.

3. 1. 2 Error Sources

The GPS positioning accuracy is mainly affected by the tropospheric propagation delay, ionospheric propagation delay, ephemeris error, and multipath error. The effects of these error sources will be discussed in order in this section.

First, the tropospheric delay caused by dry atmosphere depends only on the temperature and the atmospheric pressure at the ground, and its magnitude can be calculated with an accuracy in millimeter order. On the other hand, it is difficult to estimate the propagation delay caused by vapor because it strongly depends on the weather. Hence, around 90% of tropospheric delay is removed in general by adopting a tropospheric delay model[34]. Though the tropospheric delay is calculated by multiplying the estimated zenith delay by a mapping function, the model accuracy depends mainly on the estimation accuracy of the zenith delay. Since the zenith delay depends on atmospheric vapor, precise meteorological data is necessary to improve the estimation accuracy. In these kinematic analyses, the accuracy is not sufficient because we adopted standard values as the meteorological data. On the other hand in the static analyses with GAMIT, the zenith delay was estimated every three hours[35]. Figure 3-4 shows the time variation of estimated zenith delay. The differences of estimates between the observation sites were increasing with time. This seems to be due to the change of meteorological conditions after sunset. Note that the zenith delay estimate of the Shizuoka site seems to change independently of the other sites. These variations of zenith delay were taken into account in the static survey with GAMIT while the fixed standard values were used in KGPS. And it can be seen that the horizontal position differences hold within 1cm for baselines No. 1-6 while the vertical position differences increase according to the baseline length and reaches 9cm in baseline No.6. Therefore, the position differences shown in Figure 3-2 would be mainly caused by the tropospheric delay effect in KGPS positioning because the tropspheric delay mainly affects the vertical position.Furthermore, the tendencies of vertical position variations for baselines No. 5 and 6 (Figure 3-2e,f) are simi-

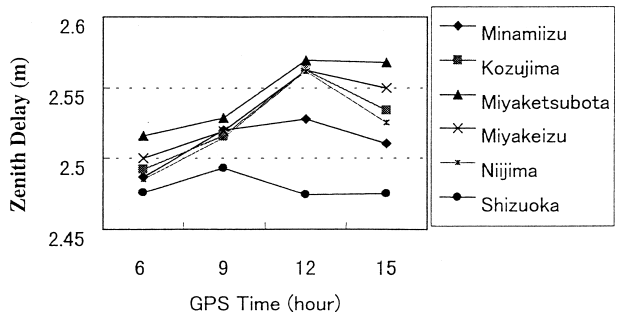

Figure 3-4 Position error caused by estimation error of zenith delay

lar, which may be due to the meteorological condition of Minamiizu sites included in both baselines. In fact, we cannot see a similar tendency in other baselines.

Then we simulate the tropospheric delay effect on positioning. Figure 3-5 shows the position errors assuming that the zenith delay for the reference site is correct and that of the estimation site contains 1, 2, 3, and 4cm errors. These values are calculated substituting the double difference of assumed tropospheric error into δy in Eq. (2.4-6) in which $(H^T C^{-1} H)^{-1} H^T C^{-1}$ is obtained using the real satellite constellation. It is obvious in Figure 3-5 that the tropospheric delay affects the vertical position estimate very much. The zenith delay estimate error of 1cm causes a bias error of around 2.5cm in the vertical position. This indicates that the zenith delay may differ around 1cm between the Miyakeizu and the Miyaketsubota sites even though they are on the same island, since the vertical position difference for baseline No.1 has around 2.3cm bias. One reason why the positioning accuracy degrades with increasing baseline length is that the difference in meteorological conditions between two sites would become larger with the baseline length.

Although the ionospheric delay does not affect the final solution for the dual frequency receivers, it will degrade the performance of the OTF. In this paper, the ionospheric delay is not modeled because only 50% of delay can be estimated by the models if no other measurement sensor is used[36), 37)], and inaccurate modeling rather affects the OTF performance. In order to evaluate the effect of ionospheric delay on positioning accuracy without the ionospheric modeling, the ionospheric signal described in Chapter 2.1.4 is used. The double differenced ionospheric signal is given as follows

$$\begin{aligned}\nabla\Delta\phi_I &= \nabla\Delta\phi_N - \nabla\Delta\phi_W \\ &= -2\nabla\Delta I + \lambda_N \nabla\Delta N_N - \lambda_W \nabla\Delta N_W + (\nabla\Delta d_{m,N} - \nabla\Delta d_{m,W}) + (\nabla\Delta\varepsilon_N - \nabla\Delta\varepsilon_W)\end{aligned} \tag{2.1-30'}$$

From the above equation, the double difference ionospheric delay is calculated if the L1 and L2 ambiguities are correctly resolved, although it contains the multipath error and the observation noise which are around three times as large as for the L1 carrier phase. Figure 3-6 shows the RMS values of $\Delta\nabla I$ for baselines No.1-6 calculated by using Eq. (2.1-30'). They would be approximately expressed by a function of the baseline length in the following equation

$$\nabla\Delta\bar{I}(cm) \cong 5.5 \cdot \left(\frac{l(km)}{100}\right) \tag{3.1-1}$$

The positioning errors caused by $\Delta\nabla I$ are shown in Figure 3-7. Considering Eq. (2.2-3), they are the positioning errors of widelane solutions. The positioning error of the L1 solution is equivalent to the value of Eq. (3.1-1) multiplied by $-f_2/f_1$ ($= -60/77$), namely 4.3. We calculate the RMS values of horizontal and vertical positioning error caused by ionospheric delay

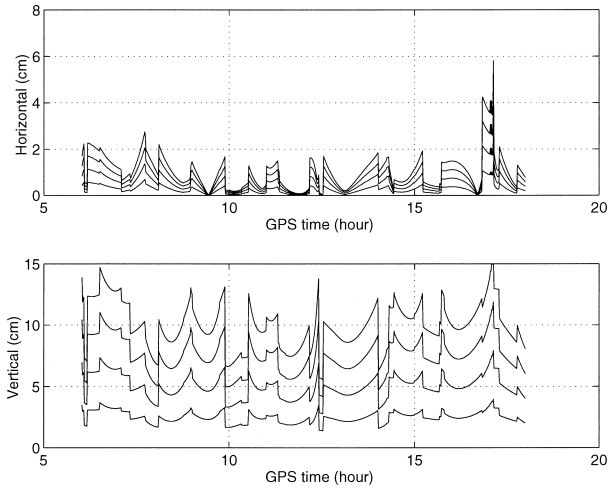

Figure 3-5 Horizontal and Vertical position errors assuming that the zenith delay for reference site is correct and that of estimation site contains 1, 2, 3, and 4cm errors

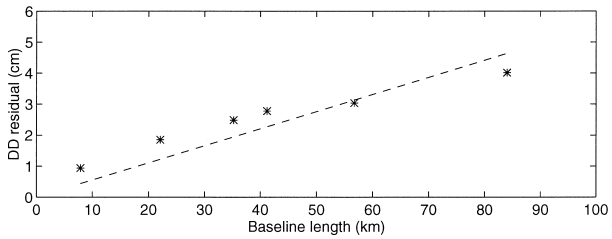

Figure 3-6 RMSs of the double differenced ionospheric errors for various baseline lengths

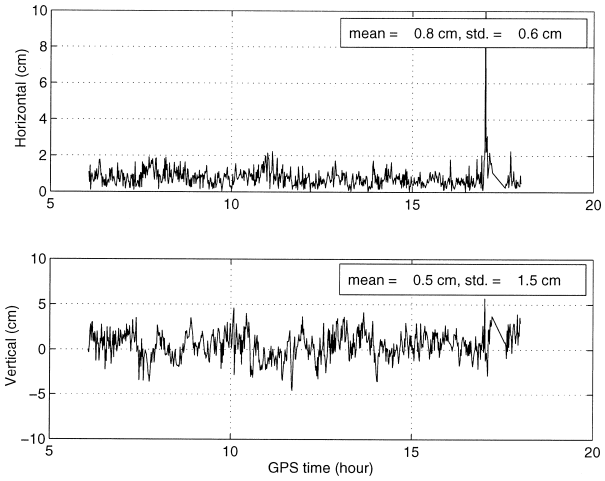

Figure 3-7a Horizontal and vertical position error caused by ionospheric delay (Miyakeizu - Miyaketsubota, 7.951km)

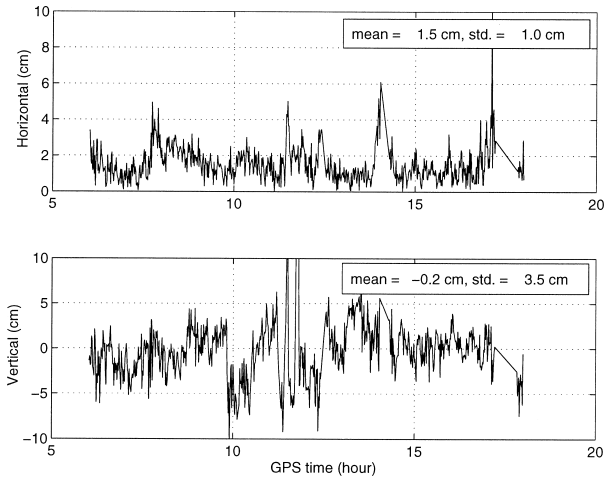

Figure 3-7b Horizontal and vertical position error caused by ionospheric delay (Niijima - Kozujima, 22.146km)

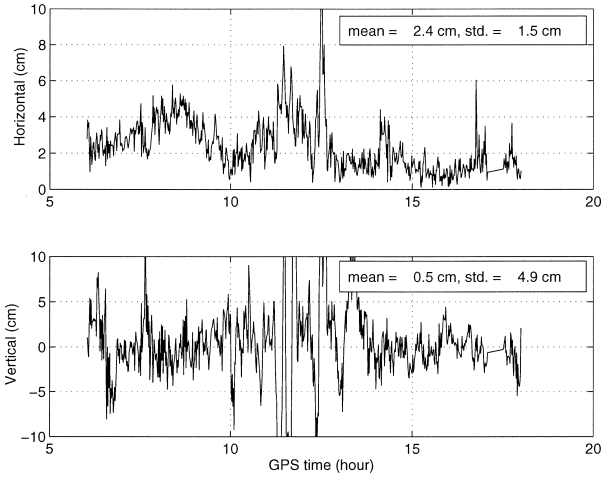

Figure 3-7c Horizontal and vertical position error caused by ionospheric delay (Miyakeizu - Kozujima, 35.182km)

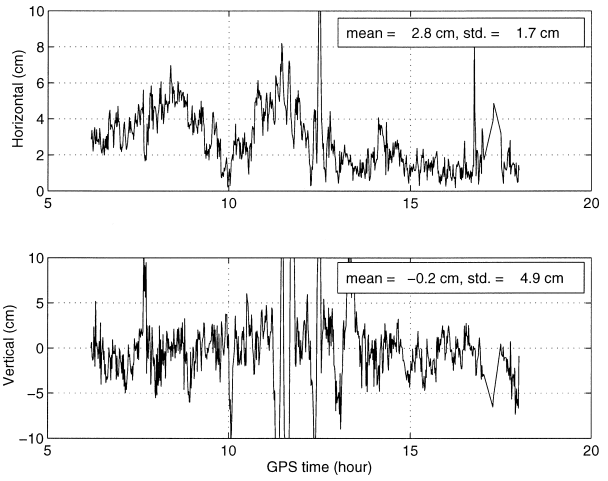

Figure 3-7d Horizontal and vertical position error caused by ionospheric delay (Miyaketsubota - Kozujima, 41.173km)

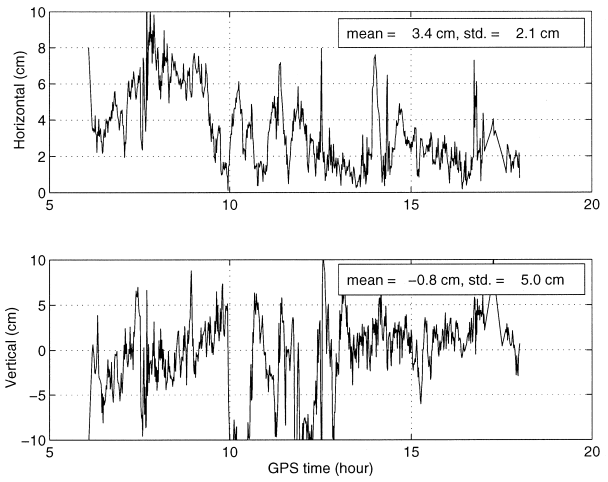

Figure 3-7e Horizontal and vertical position error caused by ionospheric delay (Minamiizu - Kozujima, 56.695km)

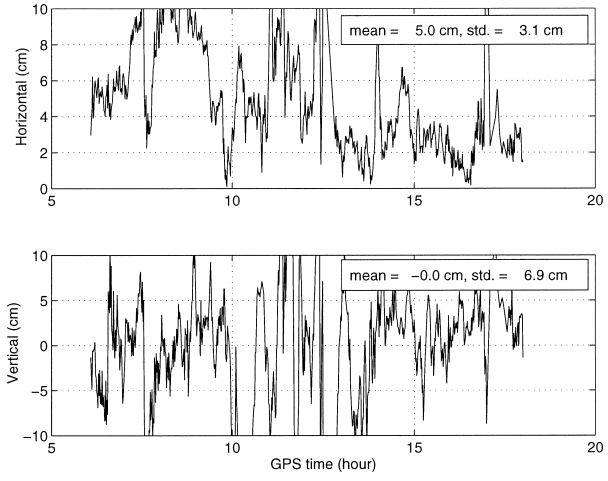

Figure 3-7f Horizontal and vertical position error caused by ionospheric delay (Minamiizu - Miyakeizu, 84.029km)

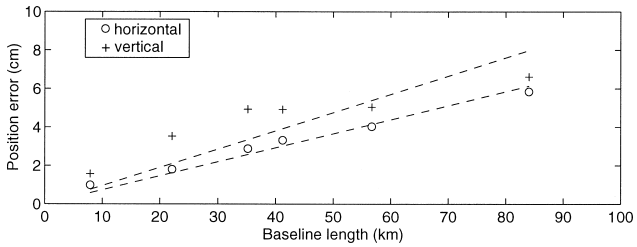

Figure 3-8 RMSs of the horizontal and vertical position errors caused by ionospheric delay

when the widelane observable was used, and show their dependence on baseline length in Figure 3-8. The approximated RMSs are given in the following equations:

$$\delta h_{ion,wide}(cm) \cong 7.3 \cdot \left(\frac{l(km)}{100}\right) \tag{3.1-2}$$

$$\delta v_{ion,wide}(cm) \cong 9.5 \cdot \left(\frac{l(km)}{100}\right) \tag{3.1-3}$$

Coefficients in the right side of the above equations are 5.7 and 7.4 for the L1 solution. Since these values are obtained by averaging the effect of ionospheric delay from 3:00 p.m. (in Japan Standard Time) to 3:00 a.m. of the next day, they vary depending on the observation time.

Next, we evaluate the effect of multipath on positioning accuracy. Multipath effect on the pseudorange is two orders of magnitude larger than on the carrier phase. It amounts to 15m even for a weak multipath signal whose relative amplitude is at -20db and sometimes to over a hundred meters when the relative amplitude of multipath is strong[38]. In those cases, since it is almost impossible to resolve carrier phase ambiguities, multipath errors should be mitigated by using an antenna with a groundplane, or changing the location of the antenna. Also, the multipath effect on the carrier phase degrades the performance of OTF. Even when the ambiguities are correctly resolved, the multipath error affects the positioning accuracy. We simply simulate the magnitude of multipath error for the carrier phase, assuming that there is only one reflected signal. The direct and reflected signals are given in simplified expressions

$$\begin{aligned} A_D &= A\cos\psi_D \\ A_R &= \alpha A\cos(\psi_D + \psi) \end{aligned} \tag{3.1-4}$$

where A_D and A_R are amplitude of direct and reflected signals, and ψ_D is the phase of the direct signal. α is a damping factor which ranges form 0 to 1 and ψ is the phase shift of the reflected signal. The superposition of both signals gives

$$\begin{aligned} A_\Sigma &\equiv A\cos\psi_D + \alpha A\cos(\psi_D + \psi) \\ &= B\cos(\psi_D + \Theta) \end{aligned} \tag{3.1-5}$$

where the resultant multipath error Θ is

$$\Theta = \arctan\left(\frac{\sin\psi}{\alpha^{-1} + \cos\psi}\right) \tag{3.1-6}$$

and the amplitude of superposed signal B is

$$B = A\sqrt{1 + \alpha^2 + 2\alpha\cos\psi} \tag{3.1-7}$$

Eq. (3.1-4,5,6,7) are taken from Seeber[10]. The maximum multipath error is 90 degrees when $\alpha = 1$, i.e., the amplitude of the reflected signal is as strong as the direct signal. Therefore, the maximum errors in L1 and L2 carrier phase are about 5cm and 6cm respectively. Figure 3-9 shows the L1 and L2 carrier phase error for various damping factor α= 0.1, 0.3, 0.5, 0.7, 0.9, 0.9999. The larger the damping factor, the larger the multipath error. Figure 3-10 shows the amplitude of superposed signal,

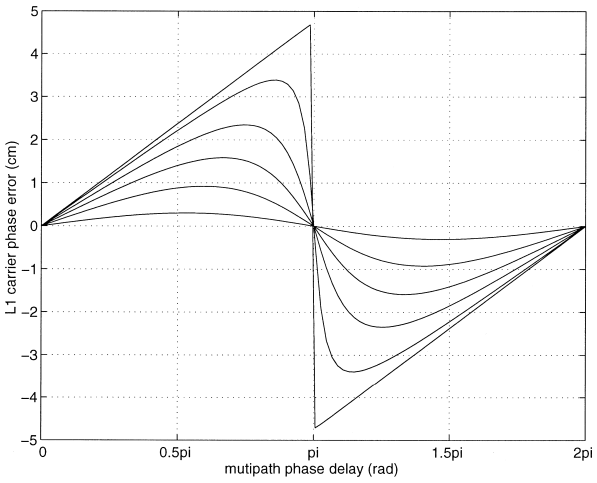

Figure 3-9a Multipath errors on L1 carrier phase for various damping factors

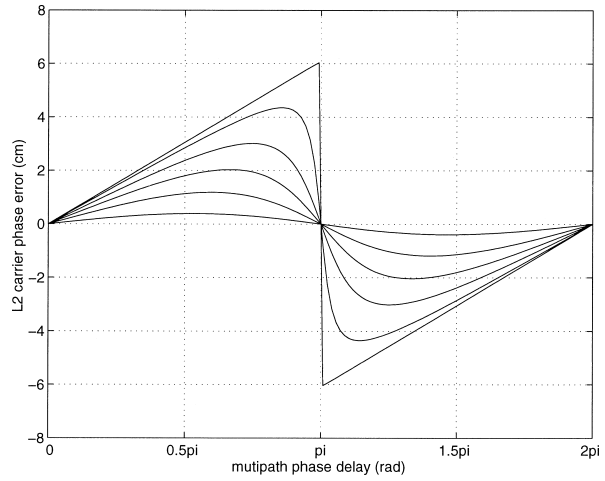

Figure 3-9b Multipath errors on L2 carrier phase for various damping factors

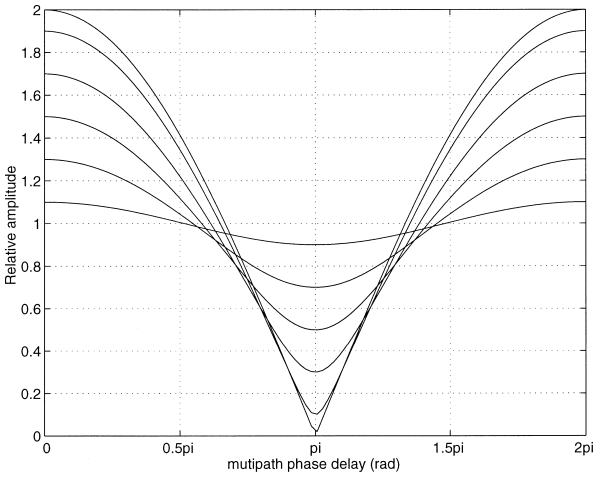

Figure 3-10 Amplitude of superposed signal for the damping factor same with Figure 3-9

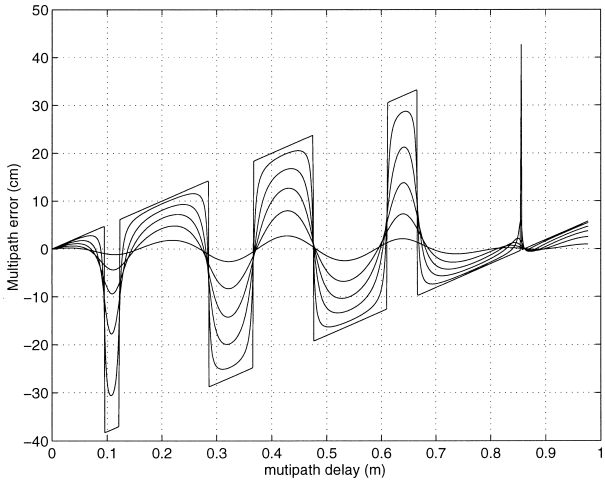

Figure 3-11a Multipath errors on widelane observable

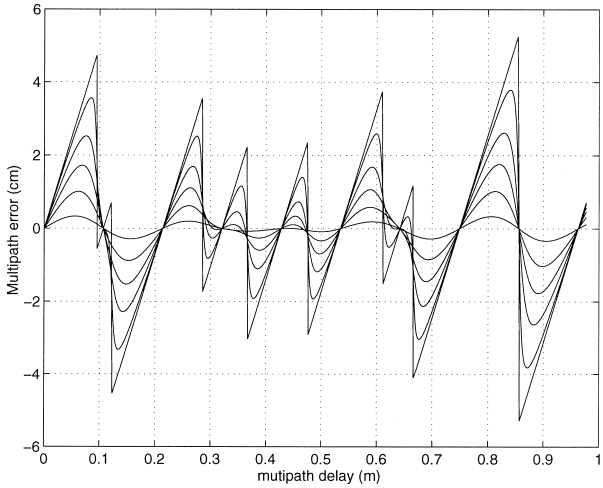

Figure 3-11b Multipath errors on narrowlane observable

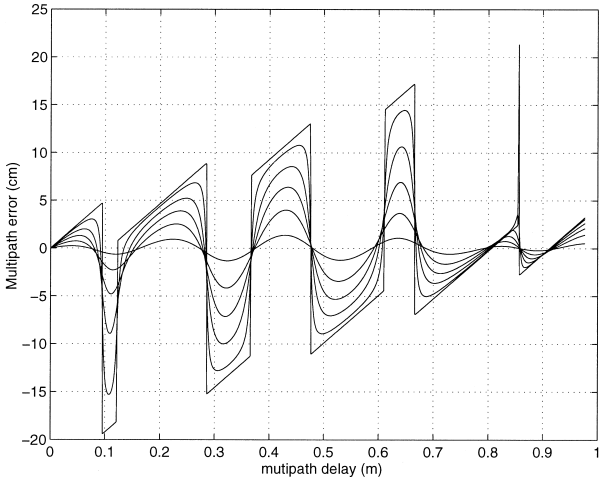

Figure 3-11c Multipath errors on ionospheric-free observabl

Table 3-2 Summary of multipath for various observable against the dumping factor

(Units: cm)

observable \ α	0.1	0.3	0.5	0.7	0.9	0.9999
L1	0.2	0.6	1.1	1.6	2.2	2.7
L2	0.3	0.8	1.4	2.1	2.9	3.5
Widelane	1.4	4.1	7.1	10.3	14.3	17.4
Narrowlane	0.2	0.5	0.9	1.3	1.8	2.2
Ionospheric-free	0.7	2.1	3.6	5.2	7.2	8.8

B, for the same damping factor. The multipath errors for widelane, narrowlane, and ionospheric-free observable are obtained by linearly combining the L1 and L2 multipath error, and are shown in Figure 3-11 (in meters) with respect to phase shift, ψ (in meters). The signal strength of L2 carrier phase is assumed to be the same with L1 carrier. The RMSs of multipath errors are summarized in Table 3-2. It is very difficult to observe the multipath error separately from other errors such as the tropospheric delay and ionospheric delay. However, it can be seen by comparing the observed data on successive days for a very short baseline in which the propagation delays are negligible. Because the GPS satellites orbit the earth twice every sidereal day (23h 56m), they return to almost the same location four minutes earlier each day. Thus, errors thought to be multipath would show the same pattern between successive days. Some authors have reported that the multipath error shows typical periods of about 30 minutes due to the changing satellite geometry[10), 38)]. The L1 carrier multipath error in these experiments would be thought to be less than 1cm (1σ) because antennas used were with groundplanes. Multipath error does not depend on the baseline length because it is due to the location of the antenna. If we extrapolate the fitting line in Figure 3-6 toward the zero baseline length, we would estimate the position error due to the multipath error and measurement noise. Considering the typical magnitude of noise to be 2～3mm (doubled in double difference), the multipath error is sufficiently reduced to a few millimeters by using the ground plane.

Furthermore, we evaluate the effect of broadcast ephemeris error on positioning accuracy for various baseline lengths. Though the precise or predicted precise ephemeris will be used nominally for this kind of analyses, it is worthy to consider the broadcast ephemeris because it can be obtained in real time aboard. The differences between broadcast ephemeris and precise ephemeris in this experiment are shown in Figure 3-12, which are defined as broadcast ephemeris error here and about 30m in RMS. Figure 3-13 shows the variation of double differenced ephemeris error. The larger the baseline length, the larger the ephemeris error. The RMSs of double differenced ephemeris errors depending on baseline length are shown in Figure 3-14 and are calculated approximately by the following equation

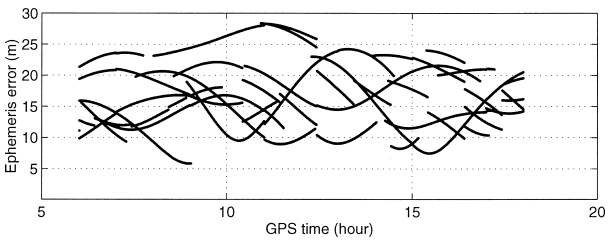

Figure 3-12 Differences between broadcast and precise ephemeris

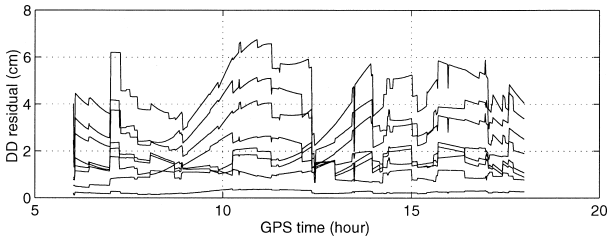

Figure 3-13 Time variation of double difference of the orbit difference (Baseline No.1-8)

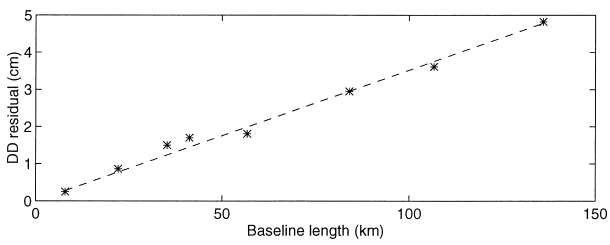

Figure 3-14 RMSs of the double differenced orbit errors depending on the baseline length

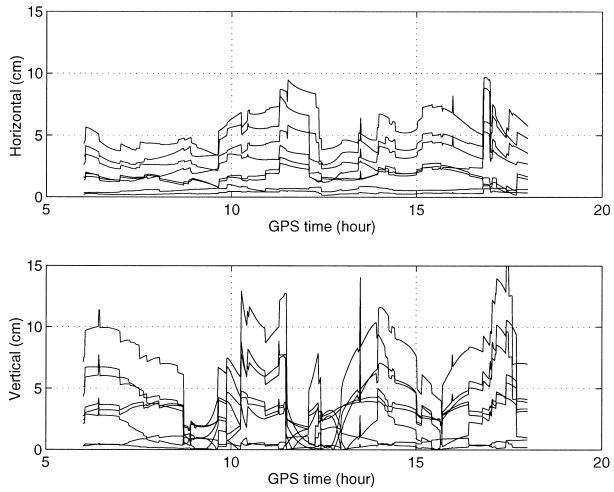

Figure 3-15 Position error caused by broadcast ephemeris error (Baseline No.1-8)

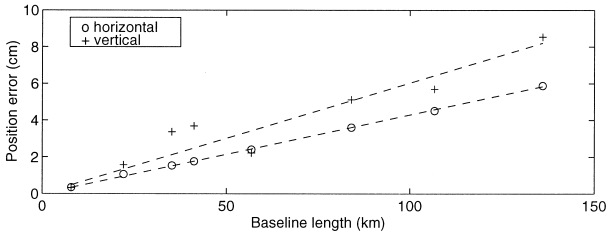

Figure 3-16 RMSs of the horizontal and vertical position errors caused by broadcast ephemeris error (Baseline No.1-8)

$$\nabla\Delta\bar{d}_{eph}(cm) \cong 3.5 \cdot \left(\frac{l(km)}{100}\right) \tag{3.1-8}$$

The horizontal and vertical positioning error caused by ephemeris error are shown in Figure 3-15 and their RMSs are shown in Figure 3-16. The least squares fittings of them give the estimates of positioning error in horizontal and vertical direction as follows:

$$\delta h_{eph}(cm) \cong 4.3 \cdot \left(\frac{l(km)}{100}\right) \tag{3.1-9}$$

$$\delta v_{eph}(cm) \cong 6.0 \cdot \left(\frac{l(km)}{100}\right) \tag{3.1-10}$$

Finally, the error budget for kinematic positioning is shown in Table 3-3. And the factors of positioning error for other observables relative to the L1 positioning error are summarized in Table 3-4, in which the signal amplitude and the measurement noise of the L2 carrier phase are assumed to be the same as those of the L1 carrier phase.

Table 3-3 Kinematic GPS measurement error budget

Error Source	Double Differenced Error (cm)	Horizontal Position Error (cm)	Vertical Position Error (cm)	Note
Tropospheric Delay	1.0	0.3	2.5	Estimation error of zenith delay is assumed to be 1cm.
Ionospheric Delay	$4.1 \cdot (l/100)$	$5.7 \cdot (l/100)$	$7.4 \cdot (l/100)$	Values for L1 carrier phase. l is baseline length (km).
Multipath	<1.0	$<1.0 \cdot$ RHDOP	$<1.0 \cdot$ RVDOP	Values for L1 carrier phase.
Broadcast Ephemeris	$3.5 \cdot (l/100)$	$4.3 \cdot (l/100)$	$6.0 \cdot (l/100)$	
Measurement Noise	0.6	$0.6 \cdot$ RHDOP	$0.6 \cdot$ RVDOP	Values for L1 carrier phase.

Table 3-4 Relative effect of GPS error sources on various observables

	Ionospheric-free	L1	Narrowlane	Widelane
Tropospheric Delay	1	1	1	1
Ionospheric Delay	0	1	1.3	1.3
Multipath	3.3	1	0.7	6.5
Broadcast Ephemeris	1	1	1	1
Measurement Noise	3.3	1	0.7	6.5

3. 1. 3 Positioning Accuracy Dependent on Baseline length

We summarize in Table 3-5 the positioning error of KGPS solutions when the L1, narrowlane, and widelane observables were used besides the ionospheric-free observable, and plot them against the baseline length in Figure 3-17. The precise ephemeris was used in kinematic positioning, and GAMIT solutions were used as the true positions. For baselines No.7 and 8, only the widelane positioning error is shown because the L1 ambiguity was not resolved for them.

It can be seen from Table 3-5 that the fact the positioning errors differ from one another for each observable is mainly due to the effect of ionospheric delay. Actually, the position calculated by using the ionospheric-free observable is the most accurate solution in general. The vertical position error for baselines No.5 and 6 is worse than for shorter baselines. One possible reason is that those baselines contain the Minamiizu site that belongs to Izu Peninsula while other sites are on islands. Therefore, the solutions of baseline No.5 and 6 would be affected by tropospheric delays that may differ from each other according to the weather conditions in a land area and in an island area. The variations of horizontal position are relatively small even in baselines No.5 and 6 because the tropospheric delay degrades horizontal positioning accuracy less than for the vertical direction. The ionospheric-free positioning errors in baselines No.1-4 are similar, while the positioning error for other observables increase in proportion to the baseline length. These are due to the ionospheric delay. Figure 3-18 shows the time variations of the L1, narrowlane, and widelane solutions for baseline No.3. Comparing the L1 positioning error

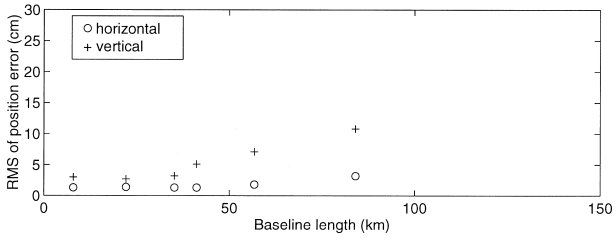

Figure 3-17a RMSs of the horizontal and vertical position errors when " ionospheric-free "observable was used (Baseline No. 1-6)

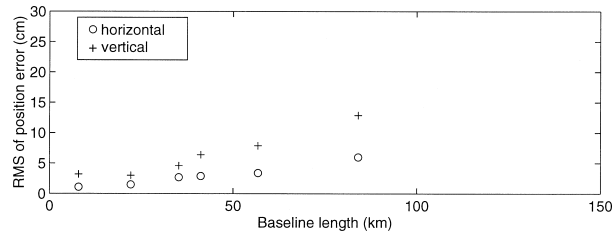

Figure 3-17b RMSs of the horizontal and vertical position errors when " L1 carrier " observable was used (Baseline No. 1-6)

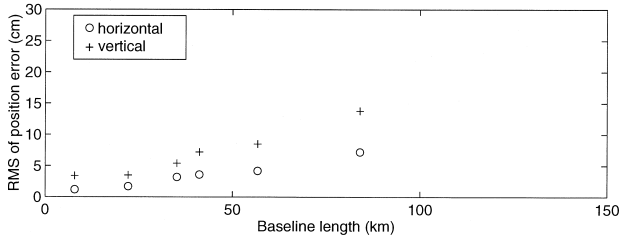

Figure 3-17c RMSs of the horizontal and vertical position errors when " narrowlane " observable was used (Baseline No. 1-6)

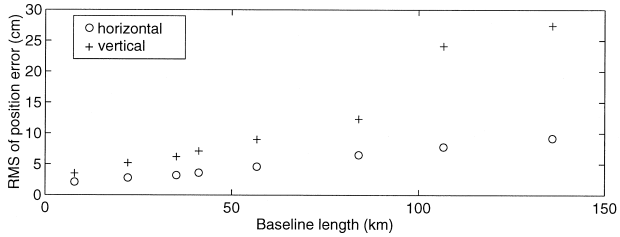

Figure 3-17d RMSs of the horizontal and vertical position errors when " widelane " observable was used (Baseline No. 1-8)

Table 3-5 Accuracy of horizontal and vertical position estimated by KGPS (RMS)

Baseline	Ionospheric-free		L1		Narrowlane		Widelane	
	Horizontal	Vertical	Horizontal	Vertical	Horizontal	Vertical	Horizontal	Vertical
1	1.3	3.0	1.1	3.2	1.2	3.4	2.1	3.5
2	1.4	2.7	1.5	3.0	1.7	3.5	2.8	5.2
3	1.3	3.2	2.7	4.6	3.2	5.4	3.2	6.2
4	1.3	5.1	2.9	6.4	3.6	7.2	3.6	7.1
5	1.8	7.1	3.4	7.9	4.2	8.5	4.6	9.0
6	3.2	10.8	6.0	12.9	7.2	13.8	6.5	12.3
7	—	—	—	—	—	—	7.8	24.1
8	—	—	—	—	—	—	9.2	27.4

(Units: cm)

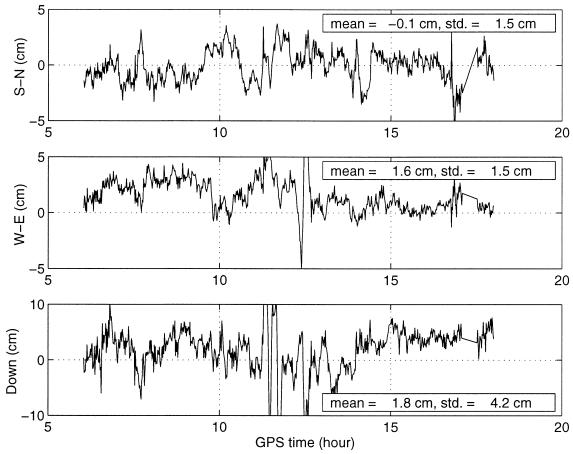

Figure 3-18a Position error in the baseline Miyakeizu - Kozujima (35.182km) when " L1 carrier " observable is used

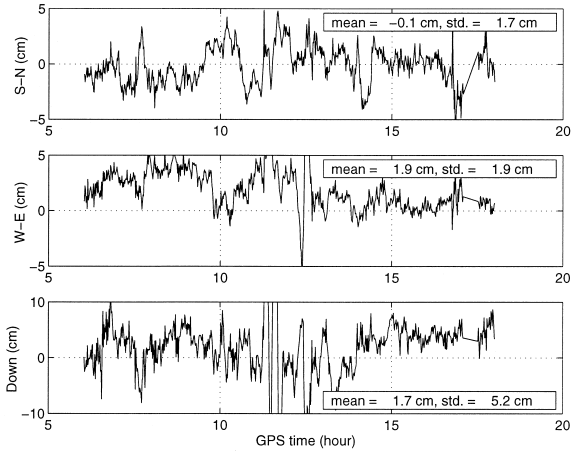

Figure 3-18b Position error in the baseline Miyakeizu - Kozujima (35.182km) when " narrowlane " observable is used

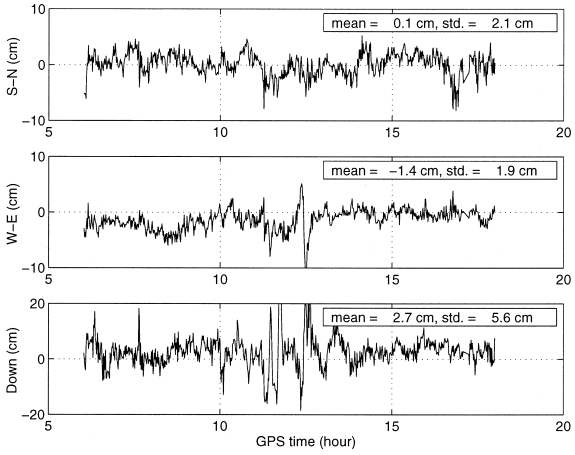

Figure 3-18c Position error in the baseline Miyakeizu - Kozujima (35.182km) when" widelane "observable is used

in Figure 3-18a with the ionospheric-free positioning error in Figure 3-2c, the large fluctuation seen from 11 to 13 o'clock in Figure 3-18a can not be seen in Figure 3-2c. Hence, it is concluded that this large error in the L1 solution is caused by the ionospheric delay.

The accuracy of the narrowlane solution is better than the L1 solution for very short baseline length where the ionospheric delay is negligible, because the measurement noise of the narrowlane is smaller. In our experiments, the L1 solution is better than the narrowlane except for baseline No.1 because the effect of ionospheric delay on the narrowlane is amplified by a factor of $f_1/f_2(\cong 1.3)$ relative to the L1 carrier.

The widelane solution is inferior to other solutions because the multipath error and measurement noises are large. However, it has the advantage that the ambiguity of the widelane can be resolved correctly for a long baseline length of over 100km. Therefore, the widelane solution could be used for various kinds of applications, for example, the AirInSar (Airborne In Synthetic aperture radar)[39], in which the precise repeat paths of aircraft are necessary.

3. 2 OTF Limit in Baseline Length

The dependence of OTF performance on baseline length will be evaluated in this section. Since the resolution of widelane ambiguity is easy for considerably long baselines (～ 100 km), we will estimate here the limit baseline length for OTF of L1 ambiguity. We should take into account several kinds of errors for OTF, such as multipath error, tropospheric delay, ionospheric delay, and ephemeris error if we use the broadcast ephemeris.

At first, we consider the test in measurement domain. Assuming that six satellites are observed, the degree of freedom is 6-4=2, and $\chi^2_{2,0.05}/df = 3.0$ in Inequality (2.2-12) if we adopt 95% as the significant level. The sum of squared measurement residuals is calculated approximately by summing the double differenced errors in Table 3-3. Hence, Inequality (2.2-12) becomes as follows in this case

$$\sqrt{1^2+4.1^2\cdot(l/100)^2+1^2} > 3.0\cdot 1 \tag{3.2-1}$$

where the first term on the left is the residual due to the tropospheric delay assuming that the difference of zenith delay estimate error between two sites is 1cm. The second term on the left is due to the ionospheric delay while the third term is the combined error of multipath and measurement noise that is assumed to be 1cm. On the right hand side, the parameter k_1^{L1} is set to 1. According to Eq. (3.2-1), the maximum baseline length in which the correct ambiguity will not be rejected is 62km. If we assumed the difference of zenith delay estimate error to be 2cm, and furthermore the ionospheric delay was as large as in the previous case, the limit baseline length for OTF would be 23km.

The test in positioning domain is considered next. Comparing Eq. (2.2-2) with (2.2-3), the effect of tropospheric delay on widelane and L1 measurement is the same. Therefore, its effect cancels if we take the difference between widelane solution and L1 solution. Since the multipath and noise are much smaller than the ionospheric delay, they can be omitted in this test. On the other hand, the effect of ionospheric delay on the position difference between widelane and L1 solutions is amplified by a factor of 2.3 because the signs of ionospheric error in measurements are opposite (see Eq. (2.2-2) and (2.2-3)). If the significant level of 95% is adopted in Inequality (2.2-13), i.e., $k_2^{L1} = 2$, and the RHDOP is set to 1.35, which is the average magnitude in this experiment, the ambiguity candidates which satisfy the following relation will be rejected.

$$\sqrt{(2.3\cdot 5.7)^2\cdot(l/100)^2} > 2\cdot\sqrt{1^2+4^2}\cdot 1.35 \tag{3.2-2}$$

According to the above relation, the maximum baseline length, in which the correct candidate will not be rejected, is 82km. If the ionospheric delay becomes two times as large as in this case, the limit baseline length is 41km. Obviously, the test in positioning domain is effective over a wider area than in the case using the test in measurement domain. Moreover, the test in measurement domain is sensitive to the meteorological condition because its performance is affected by the tropospheric delay in addition to the ionospheric delay. In fact, if the difference of zenith delay estimate error reached 3cm, all of the ambiguity candidates would be rejected by the test in measurement domain (Eq. (3.2-1)). The limits to apply the tests in both domains are summarized in Table 3-6 for various meteorological conditions. Note that these experiments were conducted at night and the solar activity was intermediate. It is expected from Table 3-6 that the limit baseline length would be reduced to about 10km if the observations were conducted in the day at a period when the sun is extremely active.

Table 3-6 Limit of the ambiguity resolution on-the-fly in baseline length

Relative estimation error of zenith delay between stations (cm)	Ionospheric delay (factor to these tests)	Limit to apply the test in observation domain (km)		Limit to apply the test in position domain (km)
		Precise ephemeris	Broadcast ephemeris	
1	1	65	49	82
1	2	32	30	41
1	3	22	21	27
2	1	49	37	82
2	2	24	22	41
2	3	16	16	27

3. 3 Detection of Crustal Movement due to an Earthquake

Finally in this chapter, we demonstrate the KGPS capability to observe the crustal movement due to an earthquake. The earthquake occurred in the sea near Kozujima at 12h43m (UTC) on 6th Oct. 1995, and its magnitude was 5.6. Figure 3-19 shows the ionospheric-free solutions for baselines No.2-5, in which the arrows show the time of the earthquake occurrence. The positioning accuracy of baseline No. 2-4 would be thought to be about 1.3cm horizontally according to the analyses of the previous day (Table 3-5). It can be seen from Figure 3-19 that Kozujima moved eastward by 2-3 cm, and this fact is consistent with the report of other authors. The movement was observed most remarkably in the baseline with Minamiizu (No.5). Although the movement before and after the earthquake can not be seen clearly in baseline No.4 and there is a bias error in the east-west direction, this may be caused by the peculiar weather of the Miyaketsubota site. On the other hand, movement in the vertical direction was not observed. We cannot judge whether or not the island moved in the vertical direction because the vertical positioning accuracy is not sufficient to detect a few centimeters of movement.

Recently, the predicted precise ephemeris are available via the Internet, which are published by the Jet Propulsion Laboratory, University of Bern, and so on. The accuracy is about 30cm for one day before prediction[40], while the ordinary broadcast ephemeris has errors of a few tens of meters. Therefore, the area where the KGPS was effective in real time would be larger if the predicted precise ephemeris were used. Furthermore, a dense GPS observation network which covers the whole of Japan has been established by the Geodetic Survey Institute[41]. The network has 610 observation sites and the average distance between the sites is about 25km (April 1996). Thus, the use of such a dense network suggests the possibility of the real time monitoring of the crustal movement by the KGPS.

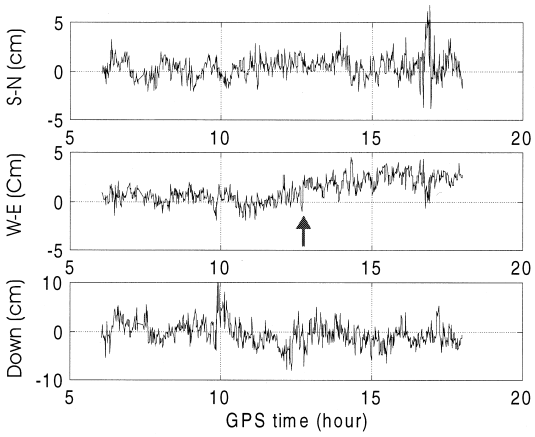

Figure 3-19a Position of Kozujima estimated by kinematic GPS before and after an earthquake (Niijima - Kozujima, 22.146km)

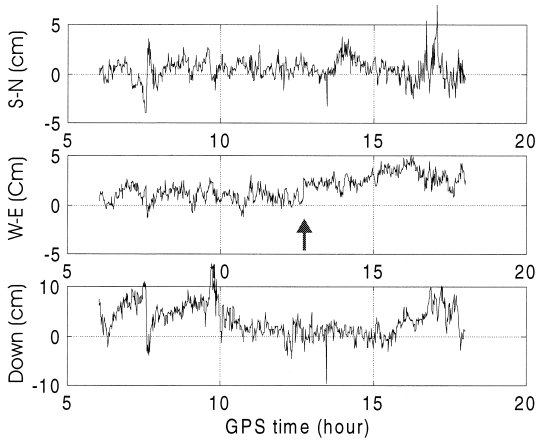

Figure 3-19b Position of Kozujima estimated by kinematic GPS before and after an earthquake (Miyakeizu - Kozujima, 35.182km)

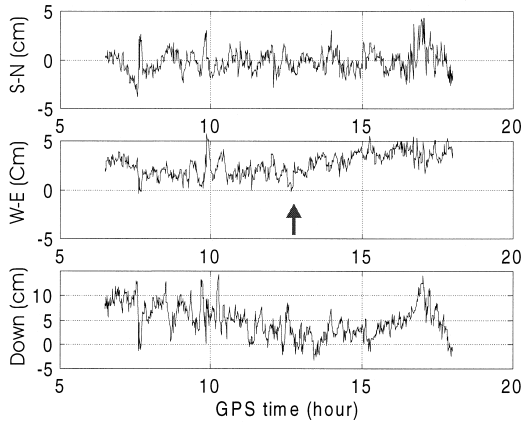

Figure 3-19c Position of Kozujima estimated by kinematic GPS before and after an earthquake (Miyaketsubota - Kozujima, 41.173km)

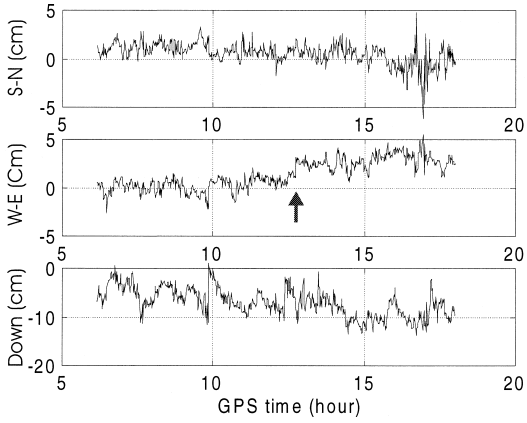

Figure 3-19d Position of Kozujima estimated by kinematic GPS before and after an earthquake (Minamiizu - Kozujima, 56.695km)

4. Flight Tests and Results

A number of flight experiments have been conducted at NAL in order to evaluate the performance of the KGPS and the attitude determination where all of the analytical software have been developed by ourselves. In this chapter, we firstly evaluate the KGPS positioning accuracy of flying aircraft by several methods, then demonstrate the performance of OTF algorithm, and finally show the results of attitude determination including the estimate of aircraft structural flexure.

4. 1 KGPS Positioning accuracy of aircraft in flight

We have already evaluated the KGPS positioning accuracy for static baselines in the previous chapter, i.e., around 1.5cm horizontally and 3.0cm vertically (1 sigma) when the baseline length is shorter than about 30km. Moreover, a comparison between our KGPS solution and the Ashtech PNAV solution showed agreement of better than 1cm[42]. Hence, we guess the positioning accuracy of aircraft in flight would be in the same level if the correct ambiguity were resolved. It is very difficult to evaluate the positioning accuracy of aircraft in flight because there is no instrument to measure the position of moving bodies with an accuracy of 10cm or better. However, we will make effort to do so by some methods. At first, we will compare some kinds of kinematic solutions and show some evidences which support the theoretically estimated accuracy. Next, we will compare the KGPS solution with the positions estimated by the laser tracking system and DGPS/INS hybrid navigation system, though these comparisons seem to be the evaluation of the laser tracker and DGPS/INS rather than the evaluation of KGPS.

4. 1. 1 Flight Test Configuration

The flight experiment was conducted at the Sendai international airport on 7 Oct. 1993. Trimble 4000SSE dual frequency GPS receivers and the research aircraft, Do-228 (Fig.4-1), were used. One receiver was installed aboard the Do-228, and another was located at a ground monitor site in the airport. Fig.4-2 shows the ground monitor site, on which a Trimble Geodetic L1/L2 antenna was mounted. The antenna was with groundplane that mitigated the multipath error, and was con-

Figure 4-1 Research aircraft Do-228 and the laser tracker

Figure 4-2 Ground monitor site, on which a Trimble Geodetic L1/L2 antenna was mounted, and the antenna of transmitter

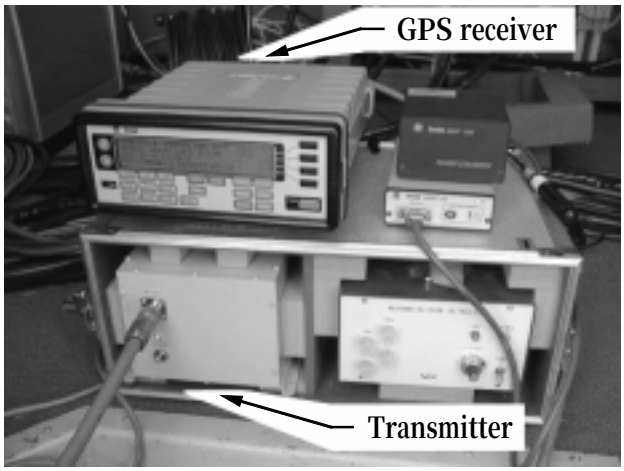

Figure 4-3 GPS receiver and the transmitter installed in the monitor site

nected to the reference GPS receiver in the monitor site as shown in Fig.4-3. The onboard receiver was connected to a Tecom MIL-E-5400 antenna mounted on the roof of the Do-228 cockpit (Fig.4-4). Applying interferometric surveying and laser theodlites, ground control points which include the locations of the monitor site and the runway thresholds were surveyed with respect to the WGS84[43]. Based on the results of this survey, the runway coordinate system (RCS) was defined and all positioning results were mapped onto this common RCS for trajectory comparison and assessment of positioning accuracy. Fig.4-5 shows the configuration of the flight experiments and the RCS coordinate system. The transmitter in Fig.4-2, 3,5 was used only for the experiments of real time DGPS/INS (Differential GPS and Inertial Navigation System) navigation to transmit the pseudorange correction data. The GPS measurements were recorded at a 2 Hz rate, and used for KGPS processing in post flight mode.

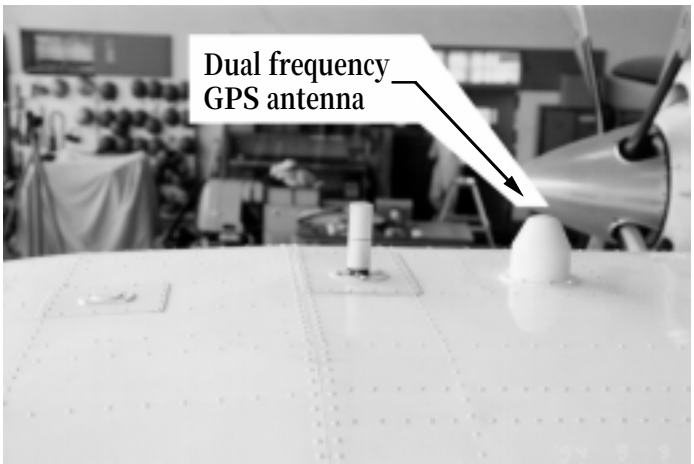

Figure 4-4 Dual frequency GPS antenna mounted on the roof of Do-228

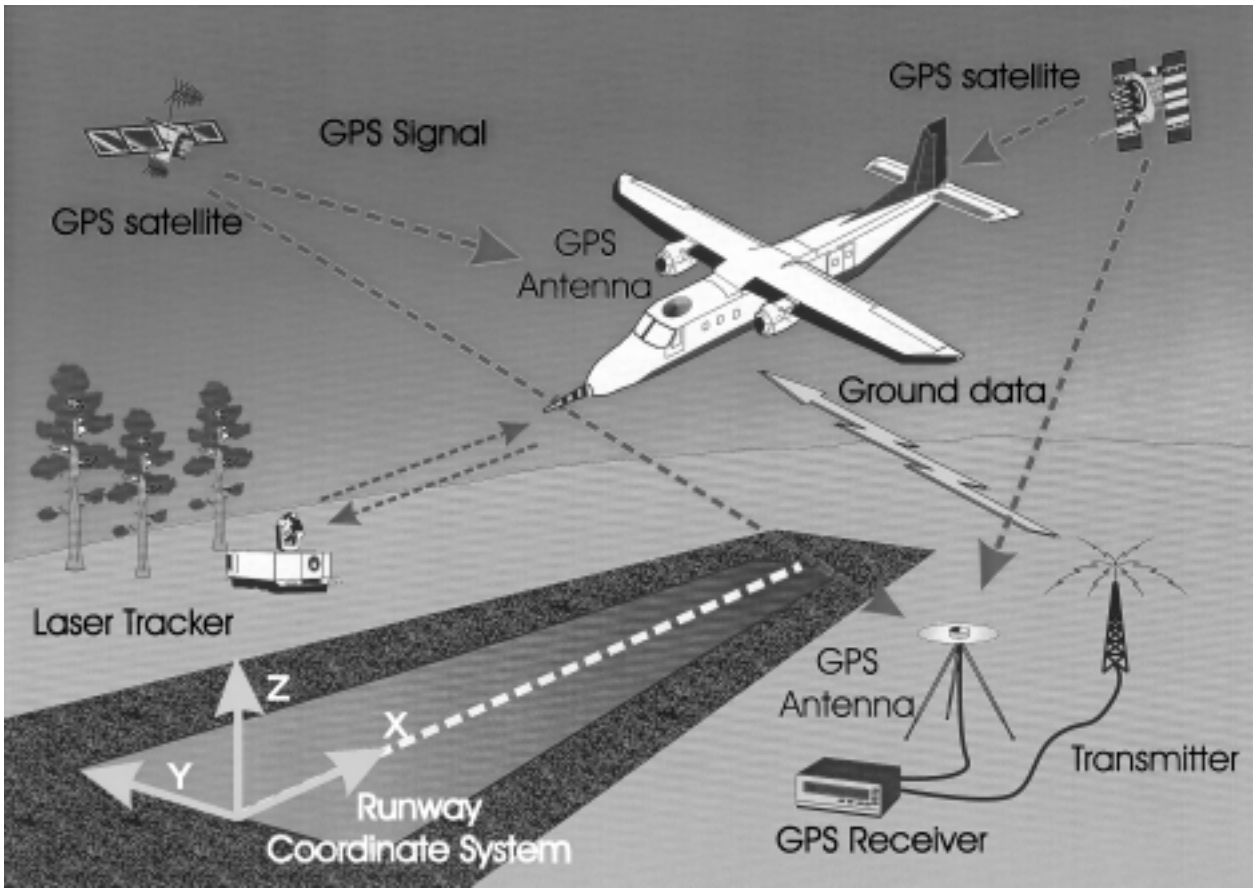

Figure 4-5 Flight test configuration and the RCS coordinate system

4. 1. 2 GPS-Estimated Flight Trajectory

In order to achieve high positioning accuracy using the carrier phase measurements, the ambiguity has to be resolved by some method. Although the OTF technique is very powerful and useful, a traditional method is used in this section. Namely, the initial and final positions of the aircraft are determined by an hour static survey, and those are used to determine the ambiguity. If new satellites are observed or cycle slips occur, the ambiguities of those satellites are determined from the antenna's position calculated using the satellites such that the corresponding ambiguities are known. The ambiguities determined by this method will be available for the evaluation of the OTF performance later.

With these pre-determined ambiguities, aircraft positions are estimated by the least squares method or the extended Kalman filter whose states are position, velocity and accelerations[44),45)]. The flight trajectory are calculated for four cases, each differing in the treatment of the propagation delay. For land based application with short baseline length (up to some 20km), double differenced ionospheric and tropospheric delays are sufficiently small to achieve high positioning accuracy and to resolve ambiguities correctly. However, in the case of the aircraft positioning, the double and even double differenced tropospheric delay would not be so small as to be neglected even with a short baseline due to the strong height dependence of the tropospheric delay. Table 4-1 summarizes the cases tested. DD and TD denote double difference and triple difference phase data respectively. In cases 3 and 4, a tropospheric delay model is implemented based on the Saastamoinen model with CfA2.2

Table 4-1 Models for the carrier phase observable

	model
Case 1	DD L1
Case 2	DD ionospheric-free
Case 3	DD ionospheric-free + trop. model
Case 4	TD ionospheric-free + trop. model

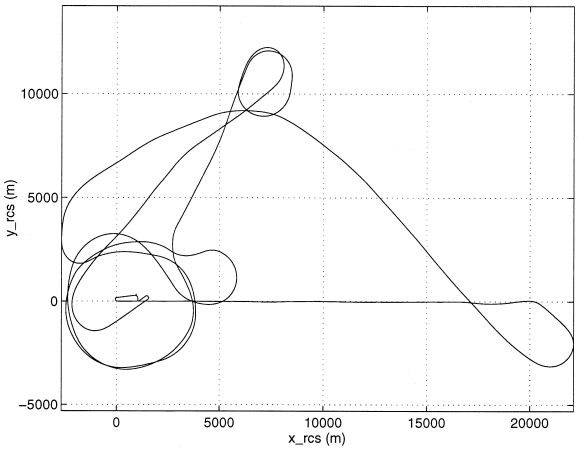

Figure 4-6 Horizontal trajectory of the aircraft

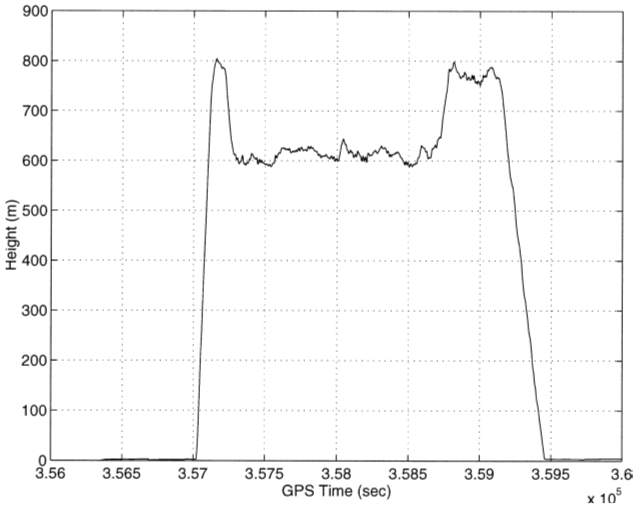

Figure 4-7 Height profile of the aircraft

mapping function with pressure and temperature gradients considered. Fig.4-6 shows the estimated flight trajectory for case 1. Positions are in a runway coordinate system whose origin is at the threshold of the runway. The X-axis is along to the runway, and the Y-axis is perpendicular to the X-axis in the horizontal plane. Fig.4-7 shows the height profile.

The measurement residuals of primary satellites for case 2 are shown in Fig.4-8 where the satellite combinations are SV18-7, SV18-24, and SV18-29. Some jumps in Fig.4-8 are caused by appearance or disappearance of satellites. The residuals for case 2 are almost the same in trends as those for case 1, but are a little noisier due to the increase of noise level by the linear combination. Of interest is to note that the residuals are larger than the measurement noise level, and have some systematic trends. Compared with the height profile (Fig.4-7), it can be seen that the trends have correlation with the height difference between reference and onboard receivers. Fig.4-9 plots position differences (Case1 - Case 2) in each of three components resolved onto the RCS. Horizontal components agree well over the experiment within a few centimeters, but height differs to an extent of 20 cm at a maximum and about 10 cm (RMS). These errors are thought to be due to the ionospheric delay error that is included in Case 1.

In order to demonstrate the effect of implementing the tropospheric delay model, we show in Fig.4-10 the residuals with the modeling. Obviously, the systematic error seen in the Fig.4-8 no longer exists. Fig.4-11 shows the position difference with/

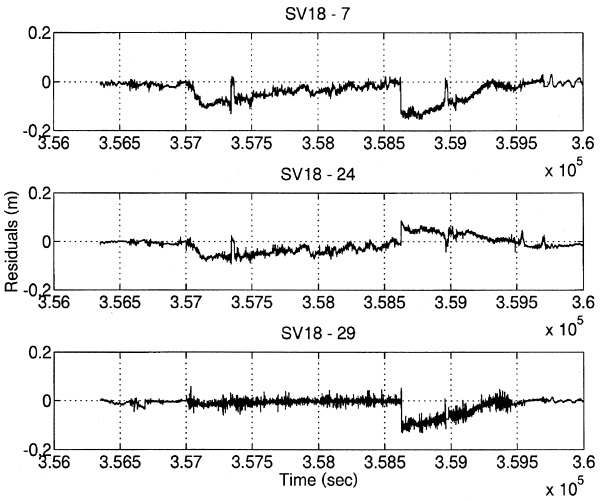

Figure 4-8 Measurement residuals of primary satellites for case 2

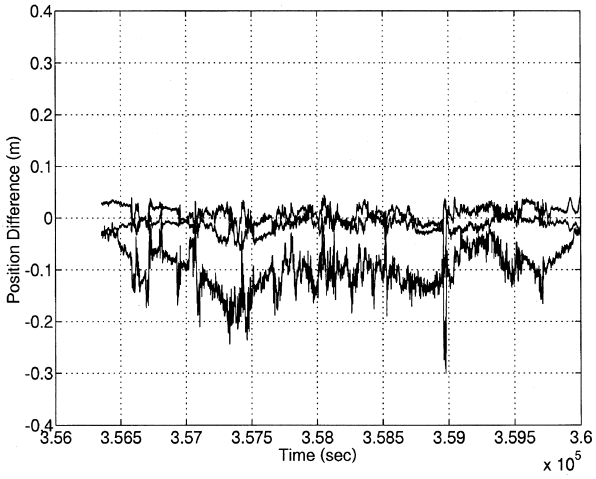

Figure 4-9 Position differences (Case1 – Case 2) in RCS coordinate

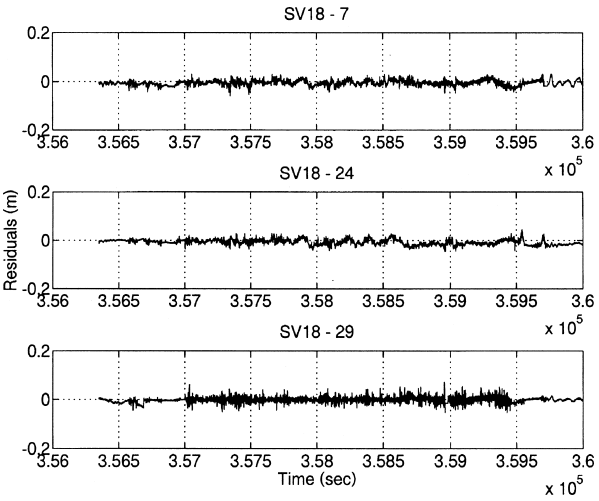

Figure 4-10 Measurement residuals with the tropospheric delay modeling for case 3

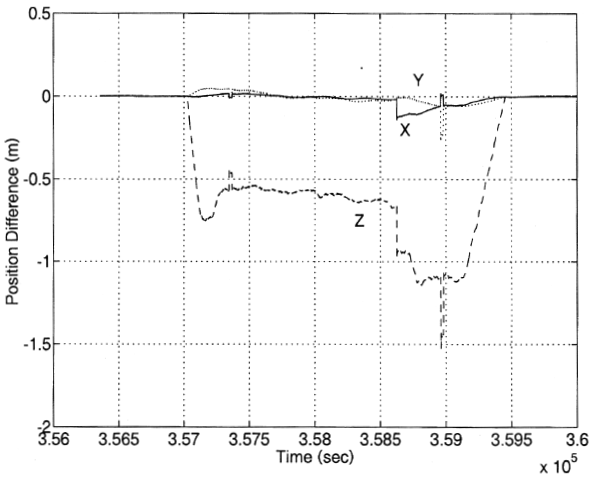

Figure 4-11 Position difference with/without tropospheric delay modeling (Case 3 – Case 2)

without tropospheric delay modeling. Horizontal differences have slightly increased but height difference has significantly expanded especially over the dynamic flight phase at a maximum of larger than one meter and with a RMS of about 60 cm.

It seems that the flight trajectory for case 3 is the most accurate among cases 1-3, because the ionospheric-free observable was used and the tropospheric delay model was also implemented. In order to verify if this is true or not, the positioning for case 4 was executed. In case 4, aircraft positions were estimated by the least squares method. The triple difference of an epoch was the time difference between double difference of the epoch and that of the previous epoch. In this experiment the time interval is 0.5 sec. Since the aircraft position of an epoch was computed relative to the position of the previous epoch, positioning error of the previous epoch would propagate to the position of the present epoch. However the final aircraft position for case 4 agrees with values obtained by static survey in 5 cm horizontally and 10 cm vertically. Therefore, the estimated aircraft position for case 4 should have maintained the accuracy of this level. Fig.4-12 shows the position difference between case 3 and 4. Since the difference is a few cm (RMS), it can be concluded that the trajectory for case 3 is accurate to within about 10 cm. This means that the ambiguity determined by the traditional method is reliably correct because even one cycle error in ambiguity during the flight would propagate to the position estimate and the final solution could not maintain such level of accuracy.

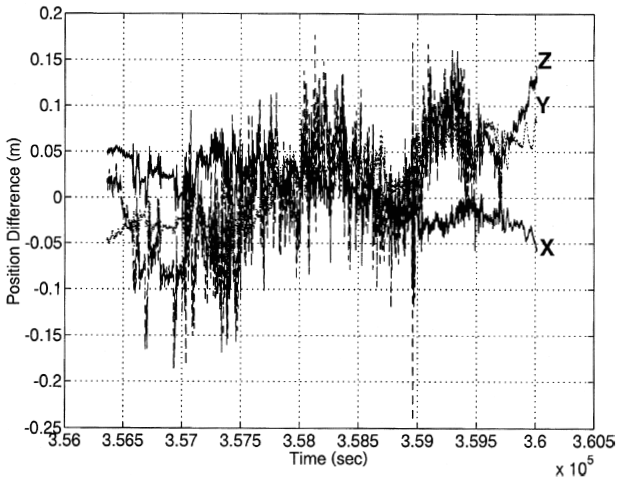

Figure 4-12 Position difference between case 3 and 4

4. 1. 3 Comparison with Laser Tracked Trajectory

In this section, we compare the KGPS trajectory of an aircraft with the position derived from the laser tracker that is a sensor system independent from GPS. The flight experiment was conducted on 15 Feb. 1995, and the experimental configuration was the same as that described in Chapter 4.1.1. The laser tracker was the Contraves ATARK MK IV (Fig.4-1), which belonged to the Electric Navigation Research Institute (ENRI). The ENRI and NAL conducted a joint research project on the evaluation of Microwave Landing System (MLS) and other navigation systems. The tracker transmits the Yag laser pulse to the reflector which is mounted on the nose of the Do-228 (Fig.4-13), and receives the return pulse. The range between the phase center of the tracker and the reflector is obtained from the propagation time. The position of the reflector is obtained from these range data, the azimuth, and elevation angles data. The accuracy of measuring the range, azimuth, and elevation angles are 0.3m (up to 23km), 0.0056 degrees, and 0.0056 degrees respectively. Therefore the positioning accuracy of the laser tracker degrades according to the distance to the reflector. For example, if the distance from the tracker to the reflector were 10km, the positioning error corresponding to 0.0056 degrees angle error would be about 1m. Fig.4-14 shows the difference between the KGPS solution and the laser tracked position[46]. The position difference between the reflector and the GPS antenna was already calibrated using the INS attitude. The gap seen around the center of Fig.4-14 was due to the lack of tracker data because the tracker couldn't always track the aircraft because of the mechanical limit. It can be seen that the position difference decreased when the aircraft approached the runway. Therefore, we would conclude that the large position difference depending on the distance was derived from the measurement error of the laser tracker's pointing angle. Comparing these two trajectories when the distance was shorter than 3 km, its mean and the standard deviation became as in Table 4-2. Those values were quite similar to the range measurement error of the laser tracker. We can conclude herein that the positioning accuracy of KGPS is better than 0.3 m for this short range. However, the accuracy would be at the same level at all distances in the local area if we considered the characteristics discussed in Chapter 3.

Also, it can be stated that the KGPS would be a useful tool to calibrate the mounting error of a laser tracker. One orbit around the laser tracker is sufficient to calibrate the local vertical and the reference angle of the azimuth. Actually, we used that method to evaluate the mounting performance by a star calibration system[47], which was applied to a laser tracker manufactured by the Hitachi Corporation. The laser tracker provided flight profiles of the ALFLEX (Automatic Landing and Flight Experiment) which was an experimental vehicle for a NAL and NASDA (National Space Development Agency of Japan) joint research project to develop an unmanned space vehicle[5].

Figure 4-13 Laser reflector mounted under the nose of Do-228

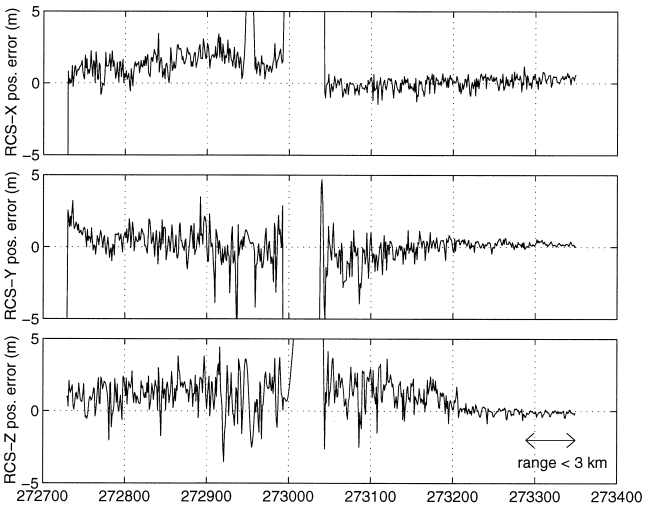

Figure 4-14 Difference between the laser and KGPS trajectory of the Do-228

Table 4-2 Differences between KGPS and laser trajectory when the distance was shorter than 3 km

	mean (m)	standard deviation (m)
X	0.32	0.27
Y	0.21	0.12
Z	-0.12	0.14

4. 1. 4 Comparison with DGPS/INS Trajectory

A DGPS/INS hybrid navigation system for the automatic approach and landing of aircraft has been developed at NAL[48]. The INS is widely used by airlines during cruise as an autonomous navigation system. However, since the INS has the disadvantage that the position error drifts a few kilometers per hour, it cannot be used for approach and landing (A/L). The instrument landing system (ILS) installed in the airport is used for precise A/L. On the other hand, GPS can give stable position information in any place. If the differential GPS technique were used, its positioning accuracy would be sufficient for precise A/L. Nevertheless, DGPS also has some disadvantages; for example, the satellite lock would be missed due to banking of the aircraft or a high dynamic maneuver, or the GPS signals would not be available due to the operation by DoD.

The DGPS/INS hybrid navigation system has been investigated to combine the advantages of the two independent systems. In addition to the non-drift precise position, the DGPS/INS provides the velocity, acceleration, attitude, and attitude rate that are essential for the aircraft control in A/L. However, its position accuracy is worse than KGPS since the DGPS/INS uses the pseudorange measurement instead of the carrier phase. Therefore the KGPS solution is used to evaluate the DGPS/INS positioning accuracy[46]. Fig.4-15 shows the position difference between KGPS and DGPS/INS at the approach. The dotted line shows the theoretical value of the DGPS/INS positioning error (2σ). The flight experiment was the same as that described in the previous section. The positioning accuracy was around 1.2m (95%) in all directions which satisfies the requirement of automatic landing. Fig.4-16 shows the velocity difference between KGPS and DGPS/INS, in which the carrier doppler measurements were used for the estimation. If the carrier doppler was not used, the velocity error was two or three times worse than shown in this figure. The dotted line shows the theoretical value of the DGPS/INS velocity error (2σ). Considering that the theoretical accuracy of DGPS/INS velocity is about 0.03 m/s, the large difference seen in Fig.4-16 is thought to be the estimate error of KGPS velocity.

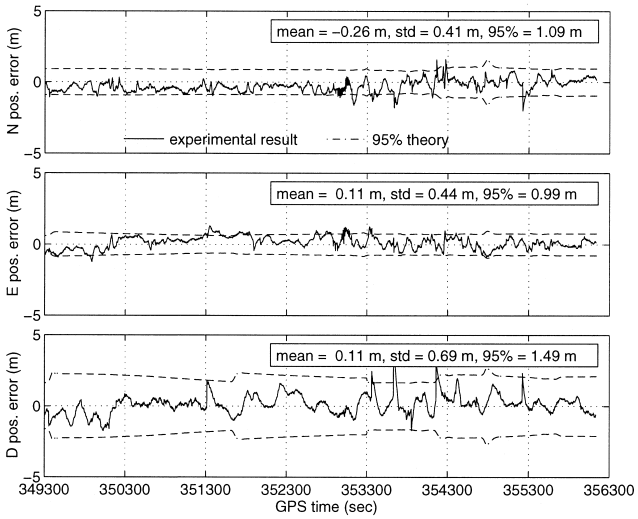

Figure 4-15 Position difference between the DGPS/INS and KGPS

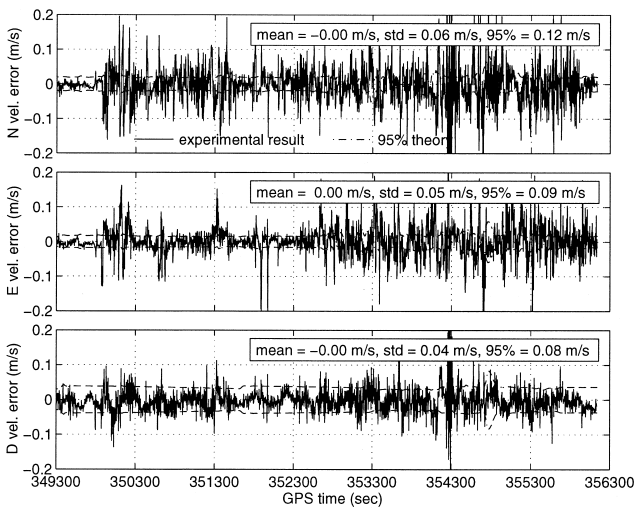

Figure 4-16 Velocity difference between the DGPS/INS and KGPS

4. 2 Evaluation of the OTF algorithm

In this section, we evaluate the performance of the OTF algorithm described in Chapter 2 using the real data of a flight experiment conducted on 8th Nov. 1994 at Sendai Airport. The flight test configuration was the same as described in Chapter 4.1.1. The trajectory of the Do-228 is shown in Fig.4-17, and the height profile is shown in Fig.4-18. The one hour of experimental data (GPS DAY[1] 313, GPS Time[2] 270571 - 274245) included 12 minutes of static data at the parking point (2 and 10 minutes before and after the flight), 41minutes of flight data, and 8 minutes of taxiing data. The flight area was within about 20km from the reference site, and the height difference is less than 800m. The change of baseline length is shown in Fig.4-19 as well. The number of satellites observed is shown in Fig.4-20, and the RDOP is shown in Fig.4-21. Furthermore, Fig.4-22 gives the elevation of observed satellites. The tropospheric delay was modeled because it is very important for aircraft applications to achieve not only high positioning accuracy but also high performance of OTF[49), 50)].

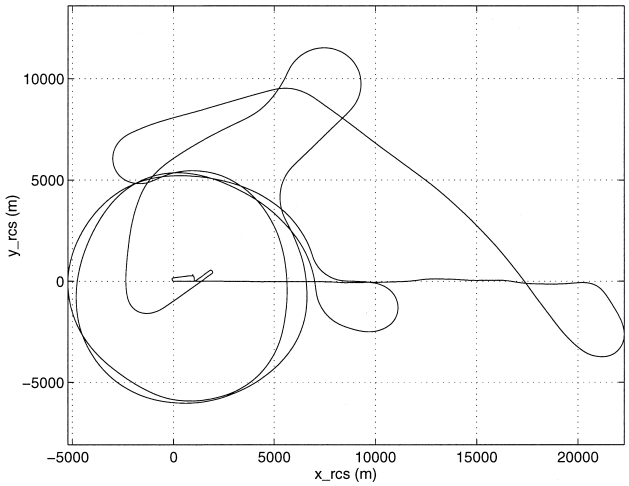

Figure 4-17 Horizontal trajectory of the aircraft

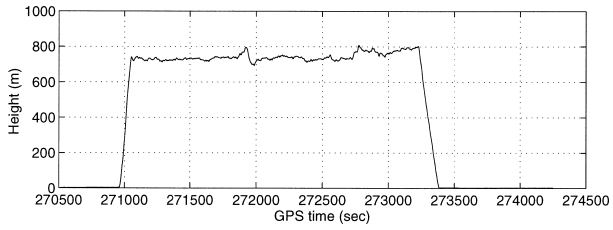

Figure 4-18 Height profile of the aircraft

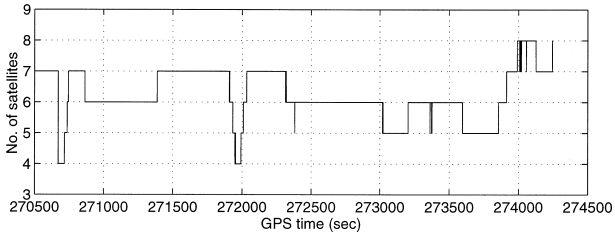

Figure 4-20 Number of satellites observed during the flight test

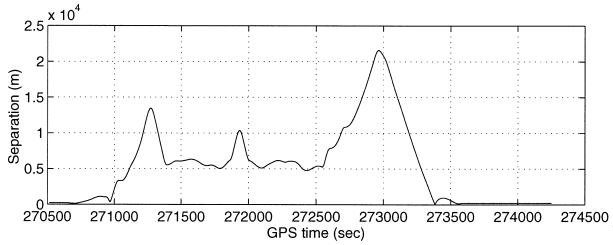

Figure 4-19 Separation between the reference receiver and the aircraft

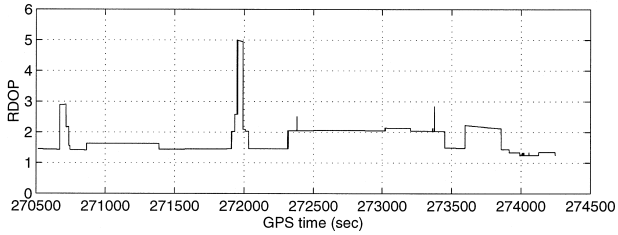

Figure 4-21 Variation of RDOP during the flight test

[1]The GPS DAY is the cumulative day from the beginning of the year.

[2]The GPS Time is the cumulative time from the begining of the week.

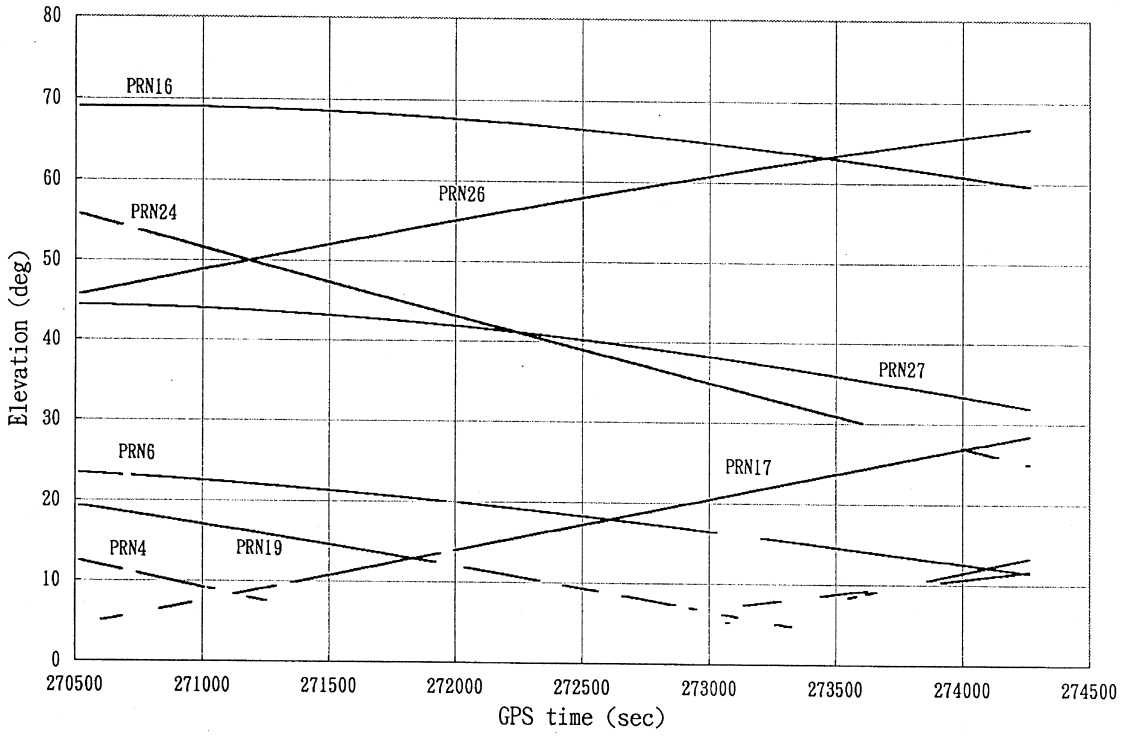

Figure 4-22 Elevations of observed satellites

At first, we show the performance of the OTF algorithm in Table 4-3 when we applied the test in measurement domain only. The series of OTF trials were performed during the whole of the experiment in a procedure in which the new trial started just after the previous trial finished. The OTF trial here means the so-called initialization in which the ambiguities of all satellites are to be resolved. In this evaluation, the maximum number of observation epochs in one trial, M, was 30 (15 seconds).

It is seen obviously from Table 4-3 that the more satellites observed the more reliable and faster the ambiguity was resolved. To resolve the L1 ambiguity is more difficult than to resolve the widelane ambiguity because the effect of several errors such as the propagation delay, multipath, and noise are relatively large for the L1 carrier phase. Note that the wavelength of the L1 carrier phase is about 19cm and is much shorter than that of the widelane. When only five satellites were observed, the possibility of obtaining the correct ambiguity was degraded considerably because the degree of freedom was small (=1). Hereafter, we will show an example of the L1 ambiguity search when five satellites were observed. The ambiguity search was performed ± 1 cycle from the initial estimate of the ambiguity so that the number of candidates was 27. Fig.4-23 shows the sum of squared residuals divided by the degree of freedom (the left side of Inequality (2.2-12)) for all candidates at GPS time 272100. The horizontal axis shows the candidate number. The five satellites (PRN 6, 16, 24, 26, 27) with the smallest RDOP were chosen though seven satellites were actually observed at the time. Since the degree of freedom is one, the value of $\chi^2_{df,1-\alpha}/df$ in Inequality (2.2-12) becomes 6.63 with the significant level of 99%. The solid line in Fig.4-23 indicates the threshold of this test. Accordingly, seven candidates were left at the time. The same test would be performed on the remaining candidates with successive measurements, and the one that was not rejected until the end would be the solution. Although the correct ambiguity set is candidate No. 14, the RSS (Root-Sum-Squares) value is minimum for candidate No. 25.

Fig.4-24 shows the residuals of double differenced L1 carrier phases for the correct ambiguity set (No.14). The satellite combinations are (PRN16-6), (PRN16-24), (PRN16-26), and (PRN16-27) respectively from top to bottom. On the other hand, Fig.4-25 gives the residuals for candidate No.25 in which the ambiguities of (PRN16-24), (PRN16-26), and (PRN16-27) have one-cycle errors. Though the residuals of the wrong ambiguity set, No.25, increase gradually according to the change of satellite constellation with time, the difference between Fig.4-24 and 4-25 could not be seen clearly until more than 5 minutes passed. In fact, the RSS of the wrong candidate was smaller than that of the correct candidate for 330 seconds. Therefore, the wrong candidate would possibly be selected as a solution in this case. In addition to the test described above, the so called 'ratio test' is often applied, in which the minimum RSS and the second minimum RSS are compared and if the ratio is larger

than 2 or 3, the candidate that has minimum RSS should be selected as a solution. However in this example, the ratio was larger than 2 for 288 seconds from the beginning. This means that the ratio test should be performed a few minutes after the beginning of the OTF trial. Considering the reasons mentioned above, it is recommended normally to perform the OTF when 6 or more satellites are observed[9].

Table 4-3a Summary of widelane OTF using the test in measurement domain only

No. of satellites	a) No. of total used epochs	b) No. of OTF trials	c) No. of solutions	d) No. of correct solutions	probability of obtaining correct solution (d/c)	average epochs required for resolution(a/d)
5	6379	4241	3846	3769	98.0	1.7
6	5117	5044	4432	4432	100.0	1.2
7	2008	1954	1303	1300	99.8	1.5

Table 4-3b Summary of L1 OTF using the test in measurement domain only

No. of satellites	a) No. of total used epochs	b) No. of OTF trials	c) No. of solutions	d) No. of correct solutions	probability of obtaining correct solution (d/c)	average epochs required for resolution (a/d)
5	6788	794	197	54	27.4	125.7
6	6195	1111	781	691	88.5	9.0
7	2743	993	954	947	99.3	2.9

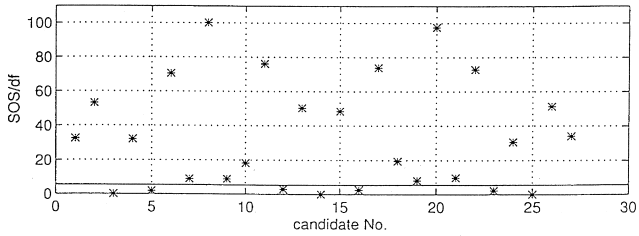

Figure 4-23 (Sum of squared residuals / degree of freedom) of each L1 phase ambiguity candidate (Solid line represents the threshold of 99%.)

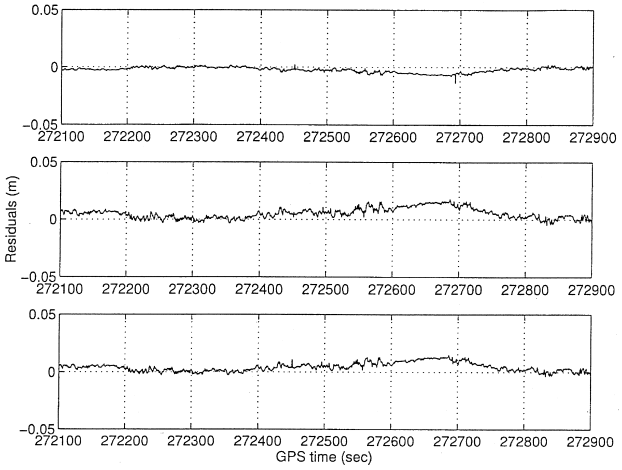

Figure4-24 Residuals of double differenced L1 phase measurement with correct ambiguities (PRN16-6, 16-24, 16-26, 16-27)

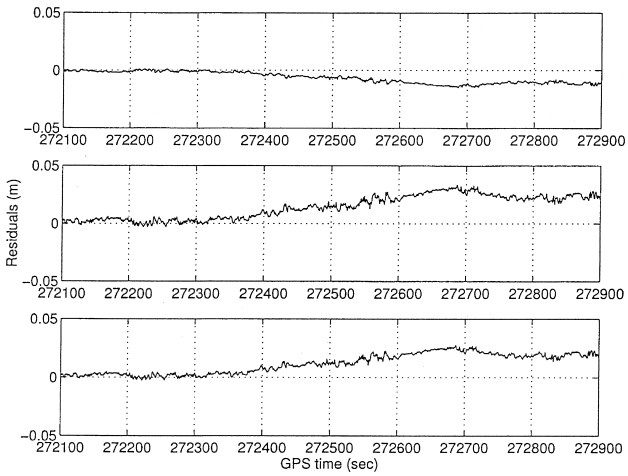

Figure4-25 Residuals of double differenced L1 phase measurement with incorrect ambiguities (PRN16-6, 16-24, 16-26, 16-27)

Next, we show the result of OTF if the test in positioning domain was performed in addition to the test in measurement domain. The result of widelane OTF is summarized in Table 4-4a, which shows little difference from Table 4-3a. This is because the difference between the pseudorange-position and the position calculated using the widelane ambiguity candidate would be considerably close to the value of σ_H^{PR-W} as seen in Eq. (2.2-17) and (2.2-18).

On the other hand, the performance of L1 OTF shown in Table 4-4b was dramatically improved. The correct ambiguity was resolved almost instantaneously with better than 99% possibility even when five satellites were observed. In the L1 OTF, if the ambiguity of a candidate had a one-cycle error, the position difference would be much greater than σ_H^{W-L1} as seen in Eq. (2.2-21) and (2.2-22). Therefore, the wrong candidates would be easily rejected. Fig.4-26 shows the distribution of the positions calculated using the smoothed pseudorange, the widelane and L1 ambiguity candidates at the time 272100, in which ×, ※, ○ stand for pseudorange, widelane, and L1 carrier phase. The position of origin was calculated using correct L1 ambiguity. In this case, the position corresponding to the correct widelane ambiguity was closest to the origin among all the widelane positions. If the difference between the position for correct widelane ambiguity and the position for a L1 candidate (○) was larger than the threshold value, the candidate would be rejected according to the test in positioning domain.

Table 4-4a Summary of widelane OTF using the tests in both measurement and positioning domains

No. of satellites	a) No. of total used epochs	b) No. of OTF trials	c) No. of solutions	d) No. of correct solutions	probability of obtaining correct solution (d/c)	average epochs required for resolution (a/d)
5	6379	4241	3846	3769	98.0	1.7
6	5117	5044	4432	4432	100.0	1.2
7	1991	1991	1645	1645	100.0	1.2

Table 4-4b Summary of L1 OTF using the tests in both measurement and positioning domains

No. of satellites	a) No. of total used epochs	b) No. of OTF trials	c) No. of solutions	d) No. of correct solutions	probability of obtaining correct solution (d/c)	average epochs required for resolution (a/d)
5	6557	6522	5597	5592	99.9	1.2
6	6170	6170	5476	5475	99.98	1.1
7	2736	2736	2616	2616	100.0	1.05

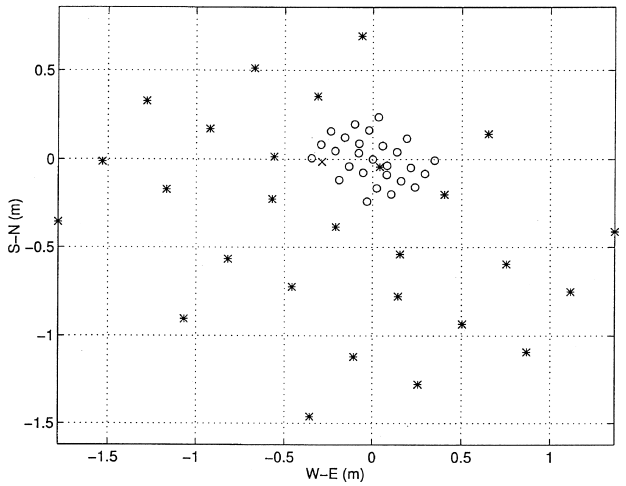

Figure 4-26 Horizontal position of the receiver using smoothed pseudorange(×), widelane ambiguity candidates(※), and L1 phase ambiguity candidates(○)

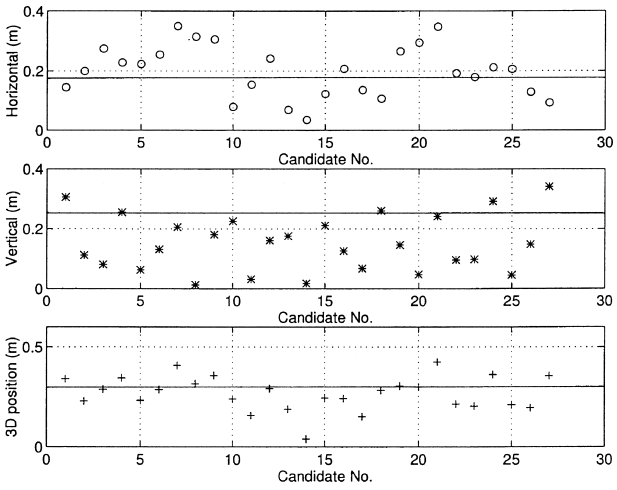

Figure 4-27 Difference between the position calculated using the correct widelane ambiguity and those using each candidate of L1 phase ambiguity

Fig.4-27 gives the horizontal, vertical and three dimensional differences between the position calculated using the correct widelane ambiguity and that using each L1 candidate, in which the solid line indicates the threshold of the test in positioning domain with a significant level of 99%. As a result, 10, 22, and 18 candidates would pass the tests in horizontal, vertical and three-dimensional positioning domain. Among these candidates, those that also passed the test in measurement domain would be retained as the candidates at the next measurement epoch. Comparing Fig.4-23 with Fig.4-27, if we considered the vertical or three dimensional position, all of the seven candidates which passed the test in positioning domain also would pass the test in measurement domain. On the other hand, only one candidate would be retained if the horizontal position were evaluated. That is to say, the correct ambiguity of the L1 carrier phase was resolved instantaneously. Thus, it becomes clear that the ambiguity can be resolved fast by evaluating the horizontal position in the positioning domain test.

In the proposed OTF algorithm, the better the accuracy of pseudorange-position is, the faster and more reliable the widelane ambiguity is resolved. Therefore, it is desirable to reduce the multipath error in pseudorange as much as possible. Recently, some GPS receivers, antennas, and software that mitigate the multipath have been developed[51),52)]. For example, the NovAtel Co. developed the narrow correlator receiver and Multipath Elimination Technology (MET) whose ranging error of pseudorange would be some tens of centimeters. Since the test in positioning domain is available even if four satellites are observed, the proposed algorithm would have a more stable performance by using such a high performance GPS receiver.

5. Summary and Conclusions

5. 1 Summary

In this paper, we proposed a new criterion for the ambiguity resolution on-the-fly, and evaluated its performance using the real GPS measurement data of the geodetic surveys and flight experiments. Furthermore, we applied the OTF algorithm to the KGPS precise positioning, and showed the experimental results.

Conclusions (1)-(4) were obtained by the analyses of surveyed GPS data in the Izu-Islands area. These experiments were conducted in order to evaluate the accuracy of kinematic GPS. Although we used static data, the results of analyses would give supporting evidence for the accuracy of moving vehicles.

(1) The horizontal positioning accuracy of kinematic GPS using the ionospheric-free observable was around 1.3cm (1σ) when the baseline length was shorter than 40km. The vertical positioning accuracy was up to 5cm for the same baselines because it is affected very much by the meteorological conditions. In order to improve the vertical positioning accuracy, detailed meteorological observations are necessary. Since the estimates of accuracy were obtained by the analyses of only one day's GPS data, the analyses of a greater number of data in various conditions will be necessary to obtain more reliable values.

(2) The L1 ambiguity was correctly resolved with a baseline of up to 80km by using the OTF algorithm we proposed. It is noted that the experiments were conducted from 3p.m. to 3a.m. local time and the activity of the sun was intermediate. The performance of OTF is much affected by the ionospheric propagation delay.

(3) In the OTF algorithm, the test in measurement domain is mainly affected by both the ionospheric and tropospheric delay, while the test in positioning domain is affected by ionospheric delay. Therefore, if only the test in measurement domain was adopted, the correct ambiguity could not be resolved due to some severe meteorological conditions.

(4) Crustal movement of a few centimeters level due to an earthquake was detected by the kinematic GPS. This result suggests the possibility of a real time monitoring of crustal movements in which the predicted precise ephemeris should be used.

Conclusions (5)-(7) were obtained by analyzing the GPS data of flight experiments conducted by NAL.

(5) As a result of comparison between the KGPS trajectory calculated using double differenced observable and that using triple differenced observable, the positioning accuracy of the former trajectory was better than 10cm (RMS).

(6) The KGPS trajectory of aircraft was compared with that calculated using the laser tracker. The RMS of position difference was 30cm, that is nearly equal to the accuracy of the tracker's range measurement. The KGPS is a very precise and useful technique for evaluating other kinds of positioning instruments such as the laser tracker and DGPS/INS navigation system.

(7) The performance of the OTF algorithm was evaluated using the data of flight experiments where the distance from the reference site was shorter than 20km and the height did not exceed 800m. The test in positioning domain would be very effective in resolving the L1 ambiguity quickly and reliably. The ambiguity was correctly resolved in two epochs with better than 98% possibility even when only five satellites were observed. Furthermore, when six or more satellites were observed, the correct ambiguity was resolved almost instantaneously with better than 99.9% possibility.

5. 2 Conclusions and Future Prospects

The kinematic GPS is a technique useful in practice to provide very accurate position information without other kinds of equipment, and some examples of off-line applications were shown in this paper. The dual frequency GPS receiver is better than a single frequency receiver because the latter has difficulty in resolving the ambiguity with baselines longer than 10km, and takes much time. In the aerial survey of the remote sensing such as SAR[39], the baseline length easily exceeds 10 km. The dual frequency receiver can give the next best position solutions for long baselines by using the widelane observable. The positioning accuracy would be better than 10cm horizontally, and 30cm vertically with baselines up to 100km which are much more accurate than the pseudorange-position. Moreover, the L1 ambiguity could be resolved easily if the widelane ambiguity was known. The proposed OTF algorithm is suited for the dual frequency receivers, and effective for fairly long baseline applications.

The next step of this study on KGPS is to establish a real time kinematic GPS (RTK) system which can be useful not only for the precise positioning of vehicles but also for the agriculture and the construction industry. Though the RTK has been developed by some organizations[53] or by some makers of GPS receivers[54),55], we have been developing the RTK for aircraft positioning using the OTF algorithm proposed above[56]. The RTK would also be applied to the aircraft navigation and A/L if its disadvantages concerning the integrity, continuity, and availability were overcome. Therefore, the real-time KGPS/INS hybrid system can be thought to be the next generation's navigation system following the DGPS/INS.

Acknowledgments

Special gratitude is expressed to ENRI and Toshiba Corporations for conducting the joint research projects. Thanks should be extended to Geographical Survey Institute and Earthquake Research Institute for affording us the geodetic survey data.

References

1) Tsujii T., M. Murata, T. Ono, K. Ishikawa, and Y. Miyazawa (1992): Flight Experiments of Differential GPS, Proceedings of the 31st SICE Annual Conference, July 22-24, Kumamoto City, pp789-790. (in Japanese)
2) Tsujii T., M. Murata, T. Ono, and K. Ishikawa (1993): Flight Evaluation of Differential GPS for Terminal Area Operations, Technical Report of National Aerospace Laboratory, TR-1210, pp1-24. (in Japanese)
3) Tsujii T., M. Murata, T. Ono, and K. Ishikawa (1995): Flight Evaluation of Differential GPS, Trans. Soc. of Instrument and Control Engineers, **31**, No.1, pp76-81. (in Japanese)
4) Harigae M., M. Murata, and T. Tsujii (1996): Orbit Determination of the Orbital Reentry Experiment (OREX) Spacecraft by GPS, Advances in the Astronautical Sciences, **93**, AAS-96-179.
5) Matsumoto S., H. Suzuki, T. Izumi, M. Harigae, T. Tsujii, K. Ishikawa, T. Ono, A Itsukaichi, H. Maeda, H. Tomita, T. Miyano: System Design and Flight Experiment Results of the Pseudolite DGPS System for Automatic Landing Flight Experiment (ALFLEX), Proceedings of ION GPS-96, Sept. 17-20, 1996, Kansas City, pp87-94.
6) Murata M., M. Harigae, and T. Tsujii (1996): Orbit Determination of the Orbital Reentry Experiment (OREX) Spacecraft by GPS, Advances in the Astronautical Sciences, **93**, AAS-96-179.
7) Hatch R. (1991): Instantaneous Ambiguity Resolution, Proceedings of IAG International Symposium No.107 on Kinematic Systems in Geodesy, Surveying and Remote Sensing. New York: Springer Verlag, pp299-308.
8) Remondi B. W. (1991): Pseudo-Kinematic GPS Results Using the Ambiguity Function Method, Navigation, J. of the Institute of Navigation, **38**, No.1, pp17-36.
9) Lachapelle G., M. E. Cannon, and G. Lu (1992): High-Precision GPS Navigation with Emphasis on Carrier-Phase Ambiguity Resolution, Marine Geodesy, **15**, pp253-269.
10) Seeber G. (1993): Satellite Geodesy, Walter de Gruyter.
11) Talbot N. C. (1991): High-Precision Real-Time GPS Positioning Concepts: Modeling and Results, Navigation, J. of the Institute of Navigation, **38**, No.2, pp147-161.
12) Ford T. L. and J. Neumann (1994): NovAtel's RT-20-A Real Time Floating Ambiguity Positioning System, Proceedings of ION GPS-94, Sept. 20-23, 1994, Salt Lake City, pp1067-1076.
13) Kleusberg A. (1986): Kinematic Relative Positioning Using GPS Code and Carrier Beat Phase Observations, Marine Geodesy, **10**, No.3, pp257-274
14) Seeber G. and G. Wübbena (1989): Kinematic Positioning with Carrier Phases and "On the Way" Ambiguity Solution, Proceedings of 5th International Geodetic Symposium on Satellite Positioning, Las Cruzes, Vol.2 pp606-609.
15) Hofmann-Wellenhof B., H. Lichtenegger, and J. Collins (1992): GPS - Theory and Practice -, Springer-Verlag.
16) Lachapelle G., M. E. Cannon, G. Lu (1992): Ambiguity Resolution on the Fly -A Comparison of P Code and High Performance C/A Code Receiver Technologies, Proceedings of ION GPS-92, Albuquerque, September 16-18, pp1025-1032.
17) Hatch R. (1994): Comparison of Several AROF Kinematic Techniques, Proceedings of ION GPS-94, Sept. 20-23, 1994, Salt Lake City, pp363-370.
18) Abidin H. Z., D. E. Wells, and A. Kleusberg (1991): Multi-Monitor Station 'On the Fly' Ambiguity Resolution: Theory and Preliminary Results, Proceedings of DGPS'91, First International Symposium on Real Time Differential Applications of

the Global Positioning System, **1**, Sept. 16-20, 1991, Braunschweig, Federal Republic of Germany, pp44-56.

19) Murata M. and M. Harigae (1992):The observations and Analysis of Selective Availability in GPS, Trans. Soc. of Instrument and Control Engineers, **28**, No.1, pp40-49. (in Japanese)

20) Remondi B. W. (1985): Global Positioning System: Description and Use, Bulletin Geodetique, **59**, pp361-377.

21) Mader G., L. (1986): Dynamic positioning using GPS carrier phase measurements, Manuscripta Geodetica, **11**, pp272-277.

22) Blewitt G. (1990): An Automatic Editing Algorithm for GPS Data, Geophysical Research Letters, **17**, No.3, pp199-202.

23) Wübbena G. (1989): The GPS adjustment software package GEONAP, concept and models. Proceedings of 5th International Geodetic Symposium, Satellite Positioning, **1**, pp452-461.

24) Tsujii T., M. Murata, M. Harigae (1995): Kinematic GPS Flight Tests - Evaluation of OTF Algorithm, Proceedings of the 34th SICE Annual Conference, July 26-28, 1995, Sapporo, pp547-548. (in Japanese)

25) Tsujii T., M. Murata, and M. Harigae (1997): First Convergence Ambiguity Resolution On-the-Fly for Dual Frequency GPS Receivers and the Flight Evaluation, Trans. Soc. of Instrument and Control Engineers, **33**, No.8, pp743-751. (in Japanese)

26) Abidin H. Z. (1993): On the Construction of the Ambiguity Searching Space for On-the-Fly Ambiguity Resolution, Navigation, J. of the Institute of Navigation, **40**, No.3, pp321-338.

27) Chen D. and G. Lachapelle (1994): A Comparison of the FASF and Least-Squares Search Algorithms for Ambiguity Resolution On-the-Fly, Proceedings of the International Symposium on Kinematic Systems in Geodesy, Geomatics and Navigation, Banff, August 30 - September 2, pp241-254.

28) Knight D. (1994): A New Method of Instantaneous Ambiguity Resolution, Proceedings of ION GPS-94, Sept. 20-23, 1994, Salt Lake City, pp.707-716.

29) Bastos L. and H. Landau (1988): Fixing cycle slips in dual-frequency kinematic GPS-applications using Kalman filtering, manuscripta geodetica, **13**, pp249-256.

30) Landau H. (1989): Precise Kinematic GPS Positioning, Bull. Geod., **63**, pp85-96.

31) Katayama T. (1983): Applied Kalman Filter, Asakura, Tokyo. (in Japanese)

32) Tsujii T., M. Harigae, and M. Murata (1997): The development of Kinematic GPS Software, KINGS, and its Application to Observations of the Crustal Movements, J. of the Geodetic Soc. Japan, **43**, No.2, pp91-105. (in Japanese)

33) Nagoya University and Shizuoka University (1996): Horizontal displacement at Kozushima detected by GPS measurements in the period 1990-1995, Rep. Coordinating Committee for Earthquake Prediction, 56, pp298-300. (in Japanese)

34) Spilker J. J. Jr. (1996): Tropospheric Effects on GPS, in Global Positioning System Theory and Applications, Progress in Astronautics and Aeronautics **164**, pp517-546.

35) MIT (Department of Earth, Atmospheric and Planetary Sciences) (1995): Documentation for the GAMIT GPS Analysis Software Release 9.40.

36) Klobuchar J. A. (1996): Ionospheric Effects on GPS, in Global Positioning System Theory and Applications, Progress in Astronautics and Aeronautics **164**, pp485-515.

37) Spilker J. J. Jr. (1996): GPS Navigation Data, in Global Positioning System Theory and Applications, Progress in Astronautics and Aeronautics **164**, pp121-176.

38) Braasch S. (1996): Multipath Effects, in Global Positioning System Theory and Applications, Progress in Astronautics and Aeronautics **164**, pp547-568.

39) Kimata F., N. Fujii, Y. Yamaguchi, T. Okuda, R. Miyajima, K. Ogawa, S. Kobayashi, H. Nohmi, M. Murata, M. Miyawaki, M. Murata, M. Harigae, and T. Tsujii (1997): Japan Earth and Planetary Science Joint Meeting 1997, Nagoya City, March 35-28, pp310.

40) Hatanaka Y. (1996): Problem of real time GPS analysis, Proceedings of the Japan symposium on GPS (1996), Tsukuba City, July 17-19, pp71-74. (in Japanese)

41) Hatanaka Y (1996): A summary of GPS meteorology, Proceedings of the Japan symposium on GPS (1996), Tsukuba City, July 17-19, pp22-25. (in Japanese)

42) Kusaba R., T. Tabei, T. Tsujii, and K. Matsushima (1997): Evaluation of GPS Kinematic Survey Using the KINGS and

PNAV, Japan Earth and Planetary Science Joint Meeting 1997, Nagoya City, March 25-28, pp307.

43) Murata M., T. Tsujii, K. Matsushima, T. Ono, Y. Miyazawa, K. Ishikawa, T. Uchida, H. Hasegawa, S. Fukushima, H. Yokoyama, H. Tajima, H. Mineno, M. Ikeuchi, M. Harigae, H. Tomita (1992): A GPS Surveying Method Applied to Approach/Landing Navigation Flight Experiments, J. of the Geodetic Soc. Japan, **38**, No.2, pp137-149.

44) Tsujii T. and M. Murata (1993): A Flight Experiment of Kinematic GPS, Proceedings of the 37th Space Science and Technology Conference, October 27-29, Kitakyushu City, pp371-372. (in Japanese)

45) Murata M., T. Tsujii, and M. Harigae (1994): Flight Experiment Results for Aircraft Positioning with Carrier Phases, Proceedings of ION GPS-94, Sept. 20-23, 1994, Salt Lake City, pp1519-1526.

46) Harigae M. (1997): Theoretical Accuracy Analysis and Flight Evaluation of DGPS/INS Hybrid Navigation System, Dr. paper, Department of Aeronautics and Astronautics, University of Tokyo.

47) Ono T., N. Okada, T. Inagaki, H., Inokuchi, M. Harigae, T. Tsujii, T. Suito, Y. Suzaki, K. Murasawa (1997): Development of the Laser Tracker and its Flight Evaluation Test, Proceedings of the 34th Aircraft Symposium, October 16-18, Tottori City, pp347-350. (in Japanese)

48) Harigae M., M. Murata, and T. Tsujii (1995): Flight Evaluation of the DGPS-INS Hybrid Navigation System for Category III Automatic Landing, Advances in the Astronautical Sciences, **91**, AAS95-622, pp771-785.

49) Tsujii T., M. Murata, and M. Harigae (1994): GPS Carrier Phase Positioning and OTF algorithms - Flight Test Results -: Proceedings of the Japan symposium on GPS (1994), December 15-16, Tokyo, pp85-90.

50) Tsujii T., M. Murata, and M. Harigae (1994): Preliminary Results of Ambiguity Resolution On-the-Fly, Proceedings of the 32nd Aircraft Symposium, October 5-7, Kitakyushu City, pp109-112.

51) Newby S. and W. Corcoran (1995): What's New from NovAtel, Proceedings of ION GPS-95, Sept. 12-15, 1995, and Palm Springs, pp133-140.

52) Kee C. and B. Parkinson (1995): Calibration of Multipath Errors on GPS Pseudorange Measurements, Proceedings of ION GPS-95, Sept. 12-15, 1995, Palm Springs, pp353-362.

53) Flodge S. L., S. R. Deloach, B. Remondi, D. Lapucha, and R. A. Barker (1994): Real-Time on-the-Fly Kinematic GPS System Results, Navigation, J. of the Institute of Navigation, **41**, No.2, pp175-185.

54) Topcon (1994): Topcon GP-R1DY GPS Receiver Operating Manual, Topcon Document Number 600260, Revision A.

55) Trimble (1995): Series 4000 Application Guide, Part Number 27249-00, Revision A.

56) Tsujii T., M. Harigae, and M. Murata (1996): Development of RTK (Real Time Kinematic GPS) system, 13th Guidance and Control symposium, Tokyo, Nov.7-8, pp39-46. (in Japanese)

TECHNICAL REPORT OF NATIONAL
AEROSPACE LABORATORY
TR-1357T

航空宇宙技術研究所報告1357T号(欧文)

平 成 10 年 10 月 発 行

発 行 所　科学技術庁航空宇宙技術研究所
東京都調布市深大寺東町7－44－1
電話（0422）47－5911　〒182－8522
印 刷 所　株 式 会 社　実 業 公 報 社
東京都千代田区九段北1－7－8

Published by
NATIONAL AEROSPACE LABORATORY
7－44－1 Jindaijihigashi－machi, Chōfu, Tokyo
JAPAN

NAL Technical Report TR-1037T

Printed in Japan